Atmospheric Research 265 (2022) 105922

Contents lists available at ScienceDirect

Atmospheric Research

journal homepage: www.elsevier.com/locate/atmosres

# Sensitivity of large eddy simulations of tropical cyclone to sub-grid scale mixing parameterization

Yubin Li [a,b], Ping Zhu [c,*], Zhiqiu Gao [d], Kevin K.W. Cheung [e]

[a] Collaborative Innovation Center on Forecast and Evaluation of Meteorological Disasters, Key Laboratory for Aerosol-Cloud-Precipitation of China Meteorological Administration, School of Atmospheric Physics, Nanjing University of Information Science and Technology, Nanjing, China
[b] Southern Marine Science and Engineering Guangdong Laboratory (Zhuhai), Zhuhai, China
[c] Department of Earth Sciences, Florida International University, Miami, FL, USA
[d] State Key Laboratory of Atmospheric Boundary Layer Physics and Atmospheric Chemistry, Institute of Atmospheric Physics, Chinese Academy of Sciences, Beijing, China
[e] Climate and Atmospheric Science, Economics and Insights Division, NSW Department of Planning, Industry and Environment, Sydney, Australia

ARTICLE INFO

*Keywords:*
Tropical cyclone
Large-eddy simulation
Boundary layer
Vertical turbulent transport
Eyewall
Parameterization of sub-grid scale processes

ABSTRACT

The surface wind structure and vertical turbulent transport processes in the eyewall of hurricane Isabel (2003) are investigated using six large-eddy simulations (LESs) with different horizontal grid spacing and three-dimensional (3D) sub-grid scale (SGS) turbulent mixing models and a convection permitting simulation that uses a coarser grid spacing and one-dimensional vertical turbulent mixing scheme. The mean radius-height distribution of storm tangential wind and radial flow, vertical velocity structure, and turbulent kinetic energy and momentum fluxes in the boundary layer generated by LESs are consistent with those derived from historical dropsonde composites, Doppler radar, and aircraft measurements. Unlike the convection permitting simulation that produces storm wind fields lacking small-scale disturbances, all LESs are able to produce sub-kilometer and kilometer scale eddy circulations in the eyewall. The inter-LES differences generally reduce with the decrease of model grid spacing. At 100-m horizontal grid spacing, the vertical momentum fluxes induced by the model-resolved eddies and the associated eddy exchange coefficients in the eyewall simulated by the LESs with different 3D SGS mixing schemes are fairly consistent. Although with uncertainties, the decomposition in terms of eddy scales suggests that sub-kilometer eddies are mainly responsible for the vertical turbulent transport within the boundary layer (~1 km depth following the conventional definition) whereas eddies greater than 1 km become the dominant contributors to the vertical momentum transport above the boundary layer in the eyewall. The strong dependence of vertical turbulent transport on eddy scales suggests that the vertical turbulent mixing parameterization in mesoscale simulations of tropical cyclones is ultimately a scale-sensitive problem.

## 1. Introduction

One of the greatest challenges in the numerical prediction of tropical cyclones (TCs) is the appropriate treatment of sub-grid scale (SGS) processes. The problem is inherent in the numerical methods that use discretized grids to simulate the continuous atmosphere. Because of the high nonlinearity of the turbulent atmospheric flow, the SGS processes result in new second-order terms in the grid-box-mean governing equations of the atmosphere to cause the otherwise closed system no longer to be closed. To close the system, additional equations that govern higher-order terms need to be provided. This is the notorious closure problem of any turbulent fluid system. In practice, these newly generated high-order terms are determined empirically based on the model-predicted lower-order moments known as SGS parameterization.

For numerical simulations with a horizontal grid-spacing greater than 1 km, sub-kilometer turbulent eddies with scales greater than Kolmogorov inertial subrange (Kolmogorov, 1941) on the eddy energy spectrum are not resolved. These energy-containing eddies are generated by the instabilities of the mean flow and obtain energy directly from the mean flow, and thus, they are fundamentally anisotropic. A common method to account for the direction-dependent turbulent transport induced by anisotropic eddies in numerical models is to implement an

* Corresponding author at: Department of Earth and Environment, Florida International University, 11200 SW 8th street, Modesto A. Maidique Campus (MMC), Miami, FL 33199, USA.
*E-mail address:* zhup@fiu.edu (P. Zhu).

https://doi.org/10.1016/j.atmosres.2021.105922
Received 22 March 2021; Received in revised form 26 September 2021; Accepted 7 November 2021
Available online 11 November 2021

SGS model built within the model dynamic solver to treat the horizontal turbulent mixing, but to have a separate one-dimensional (1D) physics module, often known as the planetary boundary layer (PBL) scheme, outside the dynamic solver to parameterize the vertical turbulent mixing. To date, a great effort has been devoted to examining the impact of vertical turbulent mixing on TC inner-core structure and intensification (e.g., Bao et al., 2012; Kepert, 2012; Li and Pu, 2008; Nolan et al., 2009; Zhu et al., 2014) and improving vertical turbulent mixing parameterization for TC prediction (e.g., Gopalakrishnan et al., 2013; Zhang and Pu, 2017; Zhu et al., 2019, and Zhu et al., 2021). There were also studies focusing on horizontal SGS mixing problems associated with TC simulations. Bryan and Rotunno (2009), Bryan (2012), and Zhang et al. (2018) investigated the sensitivity of TC intensification and structure to horizontal eddy diffusivity by adjusting the tunable mixing length. While results may vary depending on model grid spacing and specific schemes being tested, a consensus is that TC simulations at the convection permitting resolution (grid spacing roughly in a range of 1–5 km) are strongly subjected to how vertical and horizontal SGS mixing is parameterized.

As model grid spacing reduces down to the inertial subrange, large energy-containing eddies are explicitly resolved, and thus, the only eddy processes that need to be parameterized are those with scales smaller than the inertial subrange. This type of high-resolution simulation is known as large eddy simulations (LESs). The inertial subrange refers to an intermediate range of scales on the turbulent energy spectrum where the net incoming energy from larger-scale eddies is in equilibrium with the net energy cascading down to smaller-scale eddies. Eddies with scales smaller than the inertial sub-range are commonly considered to be isotropic. Because of this, in LESs the horizontal and vertical SGS mixing induced by isotropic eddies is handled by the same SGS model built within the model dynamic solver. In this case, no additional physics module is needed to treat the vertical turbulent mixing separately as it does in coarse resolution simulations. Since eddies with scales smaller than inertial subrange contain much less energy and are less flow-dependent than large energy-containing eddies, the LES methodology is commonly thought to be insensitive to formulaic details and arbitrary parameters of the SGS model, and thus, the turbulent flow generated by LESs are often used as a proxy for reality and a basis for understanding turbulent flow and guiding theories when direct observations are difficult to obtain. Indeed, LES has been making a profound impact on the boundary layer research since its first attempt by Deardorff (1970).

A key component of an LES is the SGS model for treating turbulent mixing. Smagorinsky (1963) developed the first SGS model (now known as the Smagorinsky model), which assumes that the SGS wind stresses are proportional to the gradients of corresponding wind components and the eddy diffusion coefficient itself is proportional to the local deformation of three-dimensional (3D) velocities. The SGS heat and moisture transport are parameterized in the same way and their eddy diffusion coefficients are assumed to be proportional to the eddy coefficient for momentum. While the Smagorinsky model successfully captures the shear-induced down-gradient transport of eddies, it does not include the effect of static stability on eddy transport, which may lead to large biases in strong stable and unstable conditions. In these cases, a stability correction is often added to the Smagorinsky model (e.g., MacVean and Mason, 1990) to account for the complication from the thermal stratification. Recognizing the limitation of the Smagorinsky model, Lilly (1967) and Deardorff (1980) proposed to prognostically determine turbulent kinetic energy (TKE) by adding an extra budget equation of TKE to the modeling system, and then, use the predicted TKE along with the 3D gradients of model-resolved variables to parameterize SGS turbulent transport. Since the TKE budget includes both the shear production and buoyancy production (or suppression) of TKE, this method successfully included the stability effects on SGS eddy transport. To date, both Smagorinsky-type models including those with stratification correction and TKE-type models have been widely used in various LES applications. Note that both Smagorinsky and TKE models were developed based on two assumptions: (a) local energy balance involved with shear production, buoyancy production/destruction, viscous dissipation, vertical transport, and pressure correlation; and (b) downscale energy transfer from larger to smaller eddies. Recent studies, however, show that these assumptions are not always valid. For example, under heterogeneous surface conditions or at high spatial resolutions, the advection of TKE can be significant (Lundquist and Chan, 2007). The backscatter (i.e., upscale energy transferring from smaller to larger eddies) is important near solid boundaries and in regions of strong shear and instability (Mason and Thomson, 1992; Kosović, 1997). To overcome the deficiencies of Smagorinsky and TKE models, Kosović (1997) proposed an SGS stress model to account for nonlinear backscatter and anisotropy (NBA) effects. The new NBA model was found to agree more with the theoretical profiles near the surface (Mirocha et al., 2010).

Numerical simulations of TCs at the LES resolution are rare because of the limitation in both computational resources and the methodology of LES itself. LESs in the boundary layer research are often initialized with idealized vertical profiles and forced with uniform surface conditions and horizontally homogeneous large-scale forcings. Such a modeling strategy is appropriate for small model domains of a few tens of kilometers in non-TC conditions, but it becomes questionable in TCs because a TC vortex is a moving target, and the swirling TC winds change their direction and speed continuously. This could cause the conditions at the inflow boundary of an LES domain to be substantially different from those at the outflow boundary, so that the periodic lateral boundary conditions commonly used in the classic LESs are no longer applicable. To solve this problem, Zhu (2008a) used a different approach to simulate the TC boundary layer flow by gradually scaling a real-case convection permitting simulation down to an LES domain utilizing the two-way interactive nesting technique. The nested LES in a hindcasting mode allows the roll vortices generated by the convective instability and inflection-point instability in the TC boundary layer to be explicitly simulated in a realistic TC environment (Zhu, 2008a, 2008b; Zhu et al., 2015). Their results show that the effective vertical transport of momentum, heat, and moisture induced by the explicitly resolved large turbulent eddy circulations including roll vortices cannot be well represented by the 1D PBL scheme used in the convection permitting simulations.

With the ever-increasing computational power, there are attempts of Giga-LES that has a model domain large enough to cover the entire TC vortex (e.g., Rotunno et al., 2009; Green and Zhang, 2015; Wu et al., 2018, and Li and Pu, 2021). This alleviates the problem of small-domain LESs in defining lateral boundary conditions, so that the periodic lateral boundary conditions traditionally used in LESs may be applied if the lateral boundaries of an LES are set far away from a TC vortex of interest. While the approach of using Giga-LESs to simulate TC evolution is promising, evaluation of the fidelity of the simulated TC vortex and the associated fine-scale structures resolved by LESs becomes a challenge. In the absence of decisive observational measurements, the principal method of evaluating LESs has been through sensitivity studies of individual LES models with different SGS mixing schemes or intercomparisons among different LES models. The logic is that the robustness of the simulations testifies to its fidelity. Such sensitivity tests and inter-comparison studies in the past have shed a favorable light on the LES approach in general in many meteorological applications, but they also raised questions about the ability of LES to realistically reproduce some unique features in the atmosphere, for example, the entrainment process associated with the cloud-topped boundary layer. Using 16 LESs from 10 modeling centers, Stevens et al. (2005) showed that the LES simulated global behavior of cloud-top entrainment in the region of sharp gradients at the capping inversion depends strongly on details of model numerics and SGS mixing parameterization, but the problem may be relaxed by either limiting (or turning off) the effects of SGS mixing or refining vertical resolution in the sharp gradient zone. This result challenges some of the classic arguments for rationalizing the LES

approach that the turbulent flow feature can be realistically reproduced if the energetics of large eddies are resolved.

In light of the alarming finding by Stevens et al. (2005), there is a need for examining the behavior of LES when it is applied to simulate TCs. This is because the turbulent processes in a TC environment have unique characteristics. Unlike the fair-weather or shallow cloud-topped boundary layer in which the turbulent layer is often cleanly separated from the free atmosphere above by a capping inversion, in the eyewall and rainbands, intense turbulence can extend from the boundary layer all the way up to the upper troposphere within the deep convective clouds where no physical interface exists to separate the turbulence generated by the shear and buoyancy production associated with surface processes from that generated by the cloud processes aloft due to radiative/evaporative cooling and inhomogeneous diabatic heating and cooling. However, the turbulent transport processes induced by convective clouds above the boundary layer in the eyewall of a TC remain poorly understood. Thus, one of the motivations of this study is to gain insight into the global behavior of Giga-LESs in simulating the entire deep convective eyewall extending from the boundary layer to the upper troposphere. It is expected that such an investigation can shed new light on the extent to which the underpinning of LES (namely, the supposed insensitivity of LES methodology to formulaic details) can hold in TC simulations. The second motivation is to advance our understanding of vertical turbulent transport processes above the boundary layer in the eyewall. While TKE in the eyewall has been successfully retrieved from airborne radar observations (Lorsolo et al., 2010), there is no methodology available to derive turbulent fluxes and the associated eddy exchange coefficients from airborne radar data. In-situ aircraft measurements also have difficulties to quantify in-cloud turbulent fluxes often due to insufficient resolution. Presumably, high-order turbulent moments can be quantified from the resolved turbulent flow by LESs. However, how to use the eddy correlation method to appropriately calculate turbulent moments in a horizontally heterologous TC environment has not yet been addressed. Thus, one of the focuses of this study is to discuss issues regarding the application of the eddy correlation method to the output of LESs of TCs and characterize turbulent transport processes in the eyewall. This paper is organized as follows. Section 2 describes the numerical model, experimental design, and the SGS mixing schemes used in the sensitivity tests. Section 3 presents the simulation results including validation of the simulated TC vortex against historical dropsonde composites, Doppler radar observations, and aircraft measurements, comparison between the convection permitting simulation and various LES runs, and analyses of vertical turbulent transport in the eyewall quantified from the numerical experiments. This is followed by a summary and discussion in Section 4.

## 2. Model setup, experimental design, and modeling strategy

Hurricane Isabel (2003) is simulated using the Weather Research and Forecasting (WRF) model with the Advanced-Research WRF (ARW) dynamic core (Skamarock et al., 2008). The simulations are the follow-ups of Zhu et al. (2014). Table 1 lists the seven experiments executed in this study. The configuration of the outer three domains is the same as that in Zhu et al. (2014): 8.1 km horizontal grid spacing with 375 × 289 mesh-grids (d01), 2.7 km horizontal grid spacing with 181 × 181 mesh-grids (d02), and 900-m horizontal grid spacing with 241 × 241 mesh-grids (d03). In this study, we have added two finer-scale domains. In the LES-300 experiments, a 300-m horizontal grid spacing domain with 541 × 541 mesh-grids (d04) is nested at the center of d03. Likewise, in the LES-100 experiments an additional finer-resolution domain with a grid-spacing of 100 m and 1501 × 1501 mesh-grids (d05) is nested at the center of domain d04. Fig. 1 shows the model configuration used in this study. Two-way interactive nesting is used in all experiments. A total of 74 levels are configured in the vertical for all domains in which 19 and 12 layers are below 2 km and 1 km, respectively. The vertical resolution above the boundary layer is relatively low. This is a compromise between the availability of computing resources and the number of sensitivity experiments performed in this study. The sensitivity to model vertical grid spacing will be investigated in our future study. In the convection permitting simulation, a 3D 1.5-order TKE SGS model (Lilly, 1967; Deardorff, 1980), which is built in the WRF's dynamic core, is chosen to treat the horizontal turbulent mixing. The finest grid spacing of this experiment is 900 m, meaning that the energy-containing anisotropic eddies are not resolved, thus, a 1D PBL scheme, namely, the Mellor-Yamada-Nakanishi-Niino (MYNN) 2.5 level TKE scheme (Nakanishi and Niino, 2004), is activated to overwrite the built-in 3D SGS model to account for the vertical turbulent transport. This convection permitting simulation is named as the MYNN-900 "PBL run" hereafter.

As discussed earlier, the resolved turbulent eddies become more isotropic as model resolution increases, thus, in the numerical experiments named as LES-300 and LES-100 in Table 1, the PBL scheme is not activated in domains d04 and d05 so that both horizontal and vertical SGS turbulent mixing in these two domains is handled by the built-in 3D SGS model in the WRF's dynamic core. In addition to the 3D 1.5-order TKE SGS model (Lilly, 1967; Deardorff, 1980), which is used in the MYNN-900 experiment, two other commonly used SGS models available in the WRF-ARW, namely, the 3D Smagorinsky SGS model (Smagorinsky, 1963) and the 3D NBA SGS model (Kosović, 1997), are also tested in LES-300 and LES-100 experiments. The NBA SGS stress can be calculated based on either the resolved strain-rate tensor, $\overline{S_{ij}} = \frac{1}{2}\left(\frac{\partial \overline{u_i}}{\partial x_j} + \frac{\partial \overline{u_j}}{\partial x_i}\right)$, or the prognostically predicted TKE (Mirocha et al., 2010). In this study, we chose the latter as the TKE option is more suitable to account for the buoyancy production of turbulence in the eyewall and rainbands. Detailed information of how these three models parameterize SGS fluxes is provided in the Appendix. To distinguish from the "PBL run" MYNN-900, all numerical experiments that use the 3D SGS model to treat the horizontal and vertical turbulent mixing are named as the "LES runs".

In all experiments, the MM5 similarity surface layer parameterization (Zhang and Anthes, 1982; Beljaars, 1995) is used. To properly account for surface transport processes in TC conditions, the surface exchange coefficients for drag and enthalpy proposed by Donelan et al. (2004) and Garratt (1992) respectively are activated. Other major model physics include the Rapid Radiative Transfer Model (RRTM; Mlawer

**Table 1**
Setting of numerical experiments.

| Experiments | MYNN-900 | LES-300 | | | LES-100 | | |
|---|---|---|---|---|---|---|---|
| | | SMAG-300 | TKE-300 | NBA-300 | SMAG-100 | TKE-100 | NBA-100 |
| PBL/SGS schemes | MYNN Level 2.5 PBL | 3D Smagorinsky scheme | 3D TKE scheme | 3D NBA scheme | 3D Smagorinsky scheme | 3D TKE scheme | 3D NBA scheme |
| Finest horizontal grid spacing | 900 m | 300 m | 300 m | 300 m | 100 m | 100 m | 100 m |
| Finest mesh-grids | 241 × 241 | 541 × 541 | 541 × 541 | 541 × 541 | 1501 × 1501 | 1501 × 1501 | 1501 × 1501 |
| Initiation time of the finest domain | 0000 UTC 12 September 2003 | 0100 UTC 12 September 2003 | 0100 UTC 12 September 2003 | 0100 UTC 12 September 2003 | 0200 UTC 12 September 2003 | 0200 UTC 12 September 2003 | 0200 UTC 12 September 2003 |

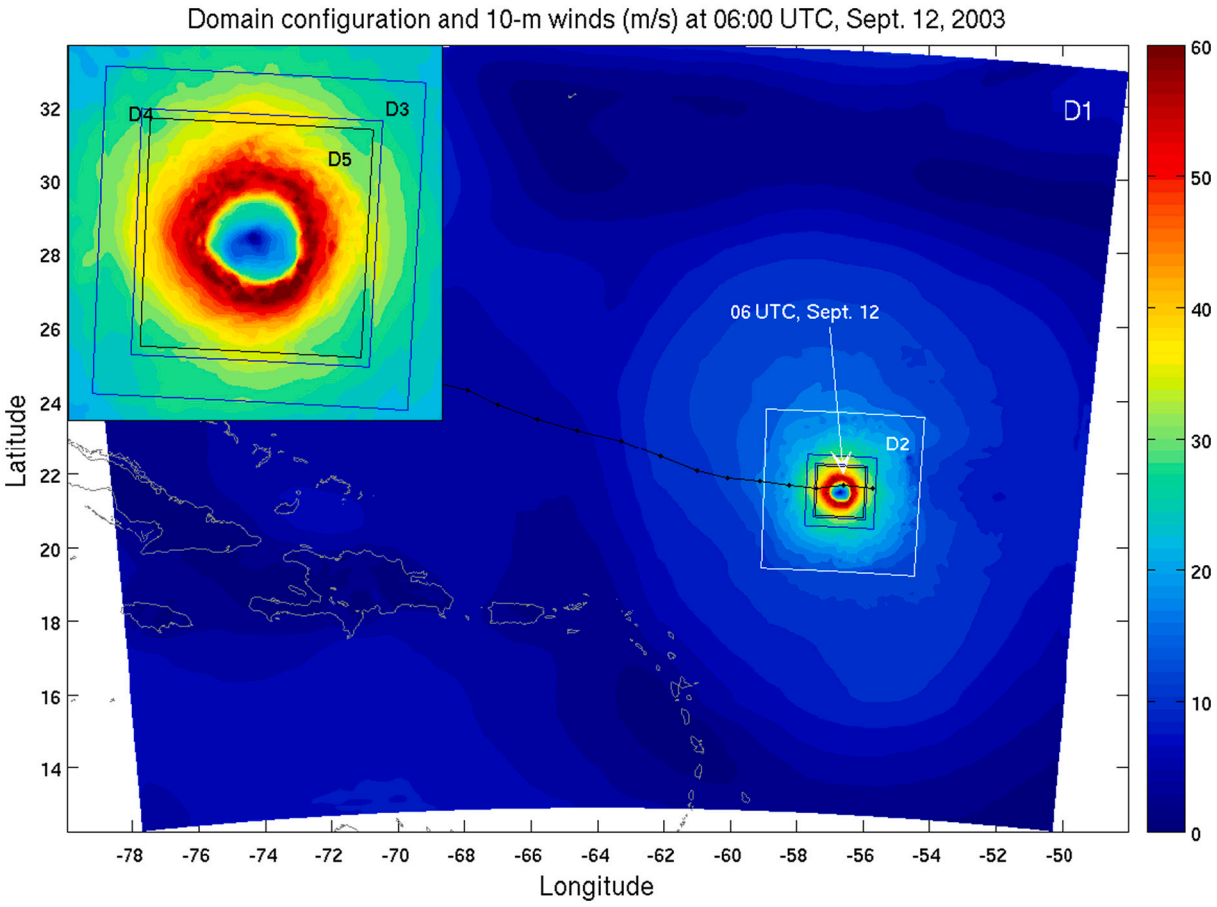


**Fig. 1.** Domain configuration of numerical simulations of Hurricane Isabel (2003). The background shows the surface wind speed at 0600 UTC on 12 September 2003 simulated by the numerical experiment of NBA-100. Domains d04 and d05 are activated in the LES-300 and LES-100 experiments only.

et al., 1997) for longwave radiation, the Dudhia scheme for short-wave radiation (Dudhia, 1989), the Thompson scheme for microphysics (Thompson et al., 2008), the thermal diffusion scheme for land surface processes (Dudhia, 1996), and the Kain–Fritsch cumulus scheme for deep convection (Kain and Fritsch, 1993). Note that the cumulus scheme is only activated in the outmost domain with a horizontal grid spacing of 8100 m. These physical schemes are kept the same in all numerical experiments.

The model initiation is the same as that described in Zhu et al. (2014). 6-hourly Geophysical Fluid Dynamics Laboratory (GFDL) model data are used to supply the initial and boundary conditions, and a bogus vortex approximately the same size and intensity as reported in real time by the National Hurricane Center (NHC) is inserted. Domains d01, d02, and d03 are initiated at 0000 UTC 12 September 2003. To shorten the model spin-up time, domains d04 and d05 are activated 1 h and 2 h later respectively (i.e., 0100 UTC and 0200 UTC) after the initiation of d01, d02, and d03. Due to the limitation of the availability of computational resources, all seven simulations end at 0800 UTC.

## 3. Results

### 3.1. Simulation validation

In this section, we provide four validation measures, namely, (a) storm intensity; (b) azimuthal-mean vortex radius-height (R-Z) distribution; (c) vertical velocity structure, and (d) turbulent momentum fluxes and TKE in the boundary layer, to examine the fidelity of the simulations performed in this study and illustrate the simulation sensitivity to model horizontal grid spacing and treatment of SGS processes.

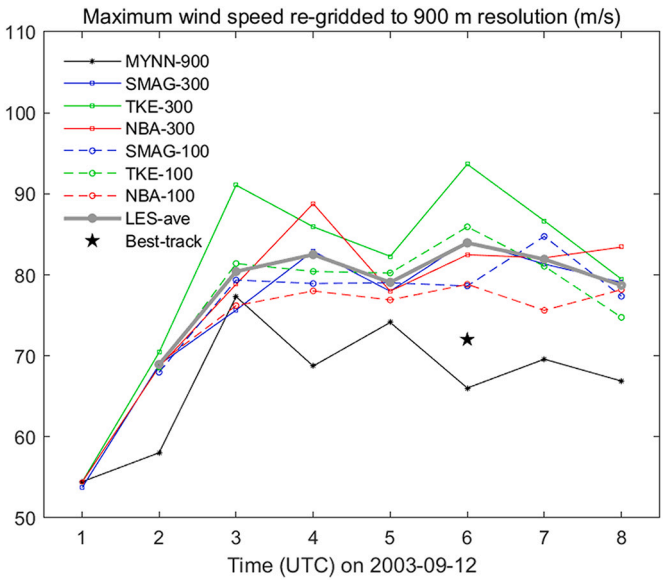


**Fig. 2.** Time series of the maximum wind speed re-gridded to 900-m resolution from the MYNN "PBL run" and various "LES runs" along with the NHC best-track data at 06:00 UTC, Sept. 12, 2003.

Fig. 2 compares the surface maximum wind speeds re-gridded to 900-m resolution (i.e., averaging over all grid points in a 900-m grid box) from various simulations with the NHC best-track data at 06:00 UTC Sept. 12,

2003. Overall, all simulations reasonably reproduced the best-track intensity. But there are apparent inter-LES differences and the difference between the MYNN "PBL run" and the mean of the "LES runs". While the "PBL run" under-predicts the best-track intensity, all "LES runs" over-predict the best-track intensity. The reasons for such differences will be discussed in detail in section 3.2.

To evaluate the structure of the simulated Isabel (2003), we compare simulations with the radar observation collected in Isabel (2003) and historical dropsonde composites. The radar retrievals (kindly provided by Dr. Jun Zhang at the Hurricane Research Division, NOAA) are from the NOAA P3 tail Doppler radar measurements collected during the N42 flight mission into Isabel (2003) during September 12–14. The radar data were processed onto the standard 2-km grids (Gamache et al., 1995; Gamache, 1997; and Reasor et al., 2013). The earliest radar data collected from this mission was at 17:19 UTC September 12, which is about 10 h later from the simulations performed in this study. Thus, an apple-to-apple comparison is not possible. However, since Isabel (2003) maintained its peak intensity of 140 Kt throughout 00–18 UTC, the radar data may provide a qualitative validation of the simulated storm. Another limitation of the radar data is that it is not available below 500 m altitude. Like the radar measurements, the dropsonde data is also not available during the simulation period since all dropsondes were collected after 16 UTC in the flight mission into Isabel (2003). Because of this, we include the historical dropsonde composites in the simulation validation. The dropsonde composites used here are from ~800 dropsondes collected in 13 TCs in the North Atlantic basin (Zhang et al. 2011b and 2020). For detailed information about the dropsonde composites, please refer to the references provided. Fig. 3 compares the azimuthal-mean tangential wind speeds as the function of height and radius normalized by the radius of maximum wind (RMW) from the seven simulations with the Doppler radar retrievals and the dropsonde composites. While all simulations reasonably produce the observed TC

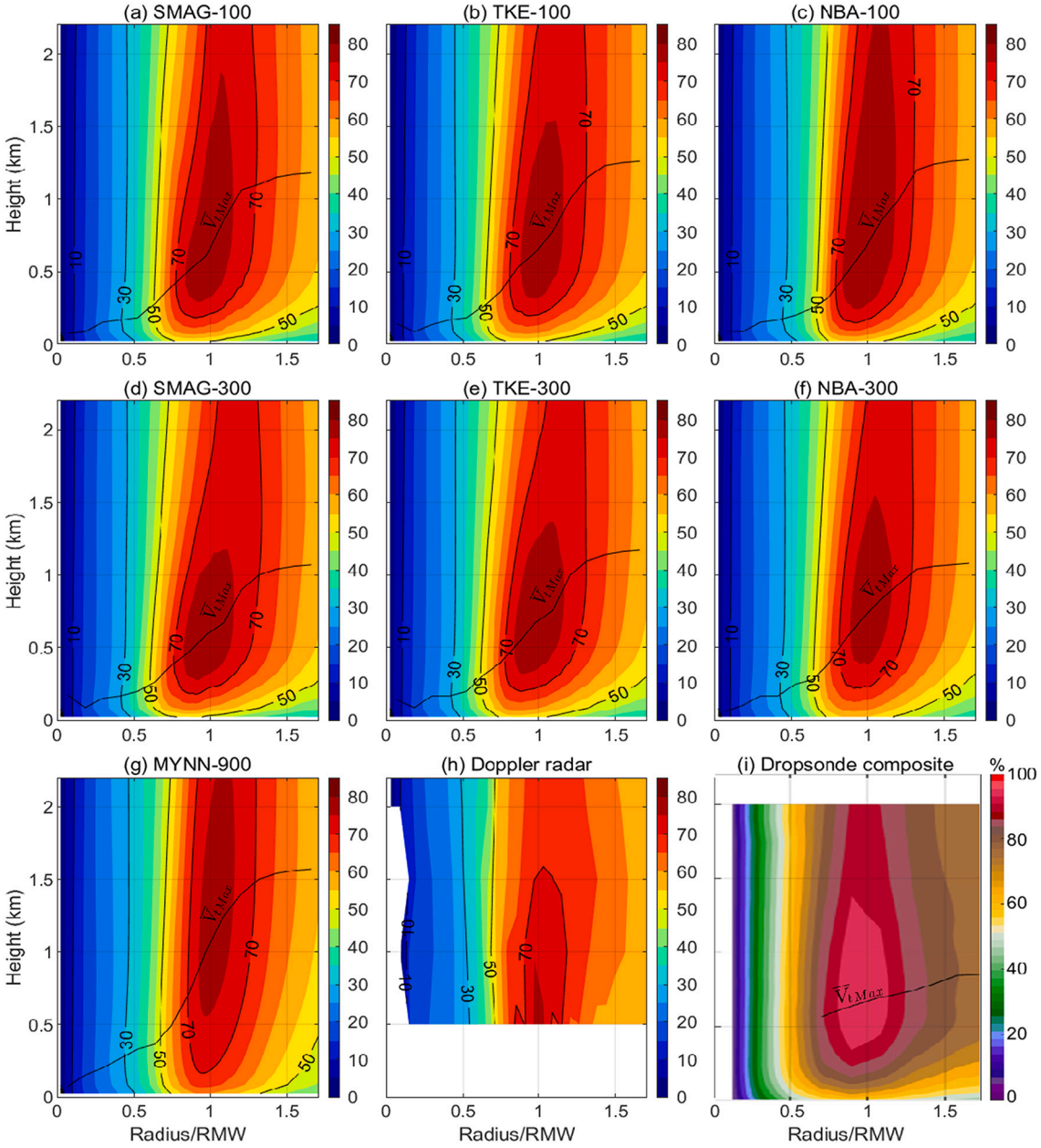


**Fig. 3.** (a) – (g): Azimuthal-mean tangential wind (m/s) as the function of height and radius normalized by RMW averaged over 03–08 UTC, Sept. 12 from the seven simulations. (h): Doppler radar retrievals at 17:19 UTC, Sept.12. (i): Dropsonde composites adopted from Zhang et al. (2011b and 2020) where the tangential winds are normalized by the maximum tangential wind $\overline{V}_{tMax}$.

vortex R-Z structure of the tangential wind with its peak wind speed occurring in the boundary layer, there is a notable difference between the "PBL run" and "LES runs". The height of the peak tangential wind in the "PBL run" (Fig. 3g) is notably higher than that in the radar retrievals and dropsonde composites. On the other hand, all "LES runs" produce the peak tangential wind heights around 500 m similar to the observations despite the different magnitudes of peak wind speeds. Note that the radial gradient of *Vt_max* near RMW is larger than that in the dropsonde composite. This might be a particular vortex structure of Isabel (2003).

The simulated and observed R-Z structure of radial flow is shown in Fig. 4. The inflow layer in the radar retrievals is much deeper than that in the dropsonde composites. It is not clear what causes this difference, and this issue will be investigated in our future study. The inflow layer depths produced by the simulations are in-between the radar observations and dropsonde composites. The six "LES runs" generate a fairly consistent inflow layer that is shallower than that in the "PBL run". This result is similar to that of Green and Zhang (2015). Dropsonde composites (Figs. 3i and 4i) show that the maximum tangential wind speed occurs inside the inflow layer just beneath the level where radial flow vanishes (i.e., $\overline{u}_r = 0$.), and the height of maximum tangential wind increases radially outward with radius. This feature is qualitatively reproduced by all "LES runs".

The contoured frequency by altitude diagram (CFAD) is often used to examine the vertical velocity structure in TCs (e.g., Yuter and Houze, 1995; Hence and Houze Jr., 2008; and Rogers and Reasor, 2013). Since the inner-most domain d5 covers an area of 75 × 75 $m^2$, to remove the possible effect from the lateral boundary conditions, we calculated the vertical velocity CFAD in an area with the radius of 58 km centered at

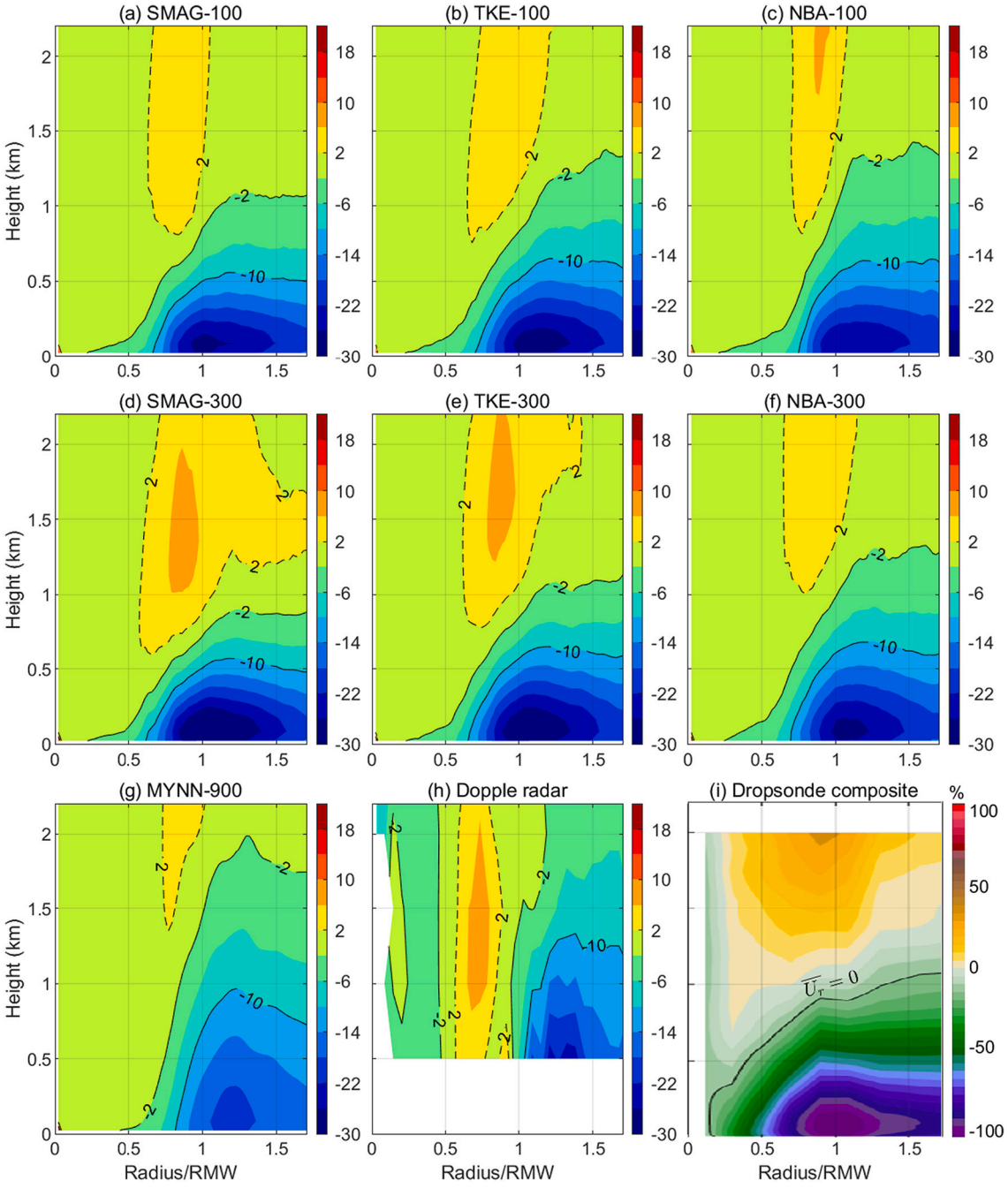


**Fig. 4.** As in Fig. 3 but for azimuthal-mean radial flow (m/s). The radial flow from dropsonde composites in (i) has been normalized by the absolute maximum radial inflow.

the storm eye. This area should be sufficiently large to examine the vertical velocity structure in the vortex inner-core region containing the eyewall and eye. Accordingly, the CFADs in the MYNN-900 "PBL run", "LES-300 runs", and radar retrievals are calculated using the data in the same area. The results are shown in Fig. 5. The CFAD calculated from the radar retrievals shows an interesting vertical structure. Narrow distributions of vertical velocity with a slight negative skewness are seen in the boundary layer, mid-troposphere around 5–6 km, and upper troposphere. A more dispersed distribution of vertical velocity, on the other hand, is seen in the low-to-mid and mid-to-upper troposphere. This vertical structure of vertical velocity shown in the radar observations is captured by all the "LES runs" with different model horizontal grid spacing and SGS models although the magnitudes vary from model to model. In contrast, the "PBL run" generates a narrow distribution of vertical velocity extending from the surface all the way up to ~8 km in altitude (Fig. 5g), indicating that the strong eyewall updrafts and downdrafts possibly associated with the eyewall 'misocyclones' or 'eyewall vorticity maxima (EVMs)' identified by airborne radars (Aberson et al., 2006; Marks et al., 2008) are not resolved in the "PBL run". Evidence on this will be provided in the following section.

In-situ turbulent flux observations in TCs, particularly those in the eyewall, are difficult to obtain due to the harsh conditions of TCs. Most of the turbulence observations in TCs were restricted to the surface wind speeds smaller than 30 $ms^{-1}$ and to the regions well outside the eyewall (Zhang et al., 2011a). For example, data from the well-known Coupled Boundary Layer Air-Sea Transfer (CBLAST) Experiment were collected mainly between the outer rainbands (Black et al., 2007; Drennan et al., 2007; French et al., 2007; and Zhang et al., 2008). To our knowledge, the published turbulence flux data in the eyewall to date include those collected by the NOAA WP-3D research aircraft during the eyewall

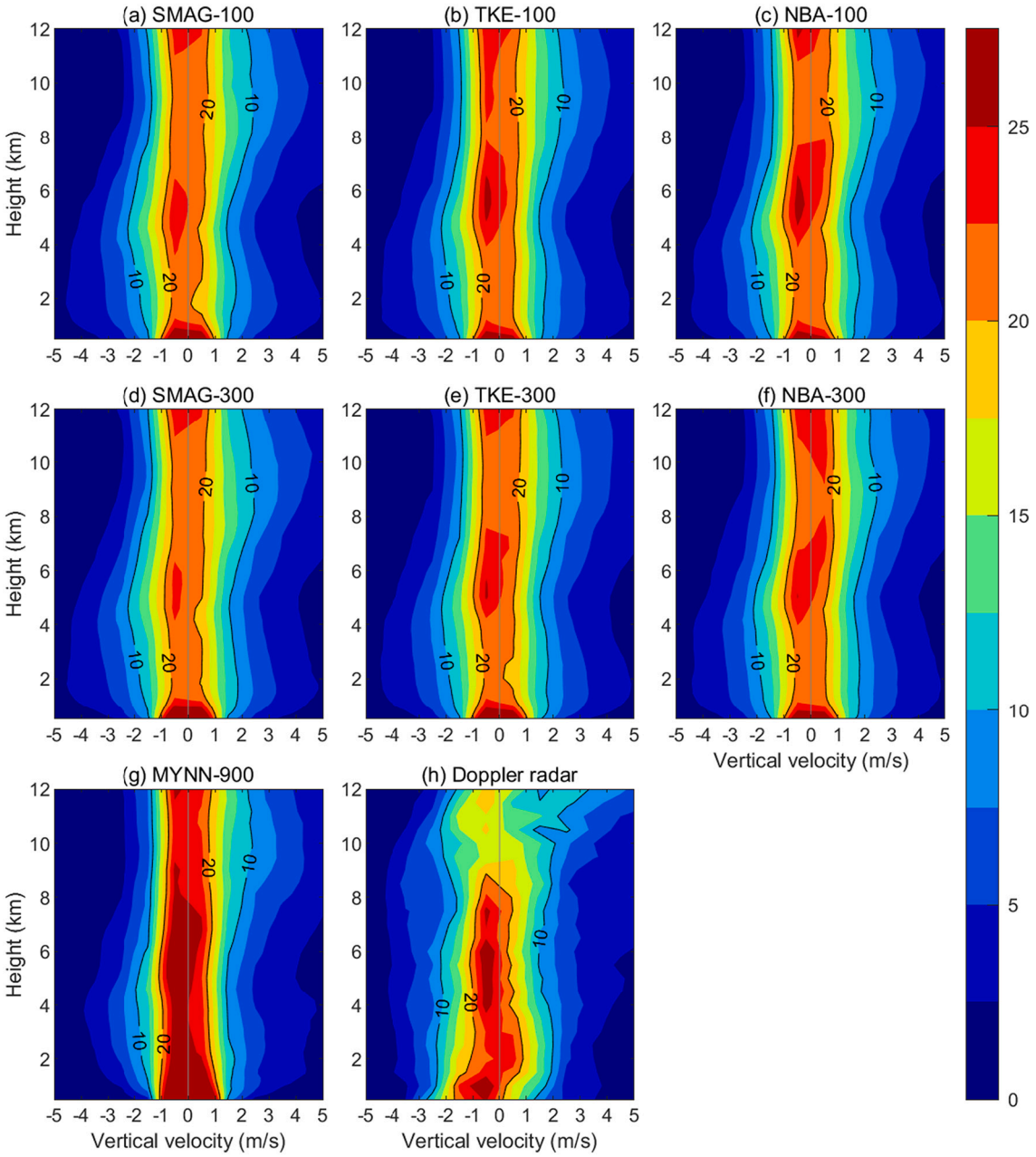


**Fig. 5.** (a) – (g): Contoured frequency by altitude diagram (CFAD) of vertical velocity in the TC inner-core region (58 km in radius) averaged over 03–08 UTC, Sept. 12 from the seven simulations. (h): CFAD of vertical velocity in the same area from the Doppler radar retrievals at 17:19 UTC, Sept.12. Vertical grey line is the zero line.

penetrations into Hurricanes Allen (1980) and Hugo (1989) (Zhang et al., 2011a); and those collected by the Coyote small unmanned aircraft system (sUAS) in Hurricanes Maria (2017) and Michael (2018) (Cione et al., 2020). There were two and four eyewall penetration legs during the reconnaissance flights into Allen (1980) and Hugo (1989); and five and one eyewall penetration sUAS flights into Maria (2017) and Michael (2018), respectively. In the absence of flux observations in the eyewall of Isabel (2003), the turbulence data collected during the eyewall penetrations into these hurricanes could serve as a good alternative for evaluating the turbulent transport in the vortex inner-core region induced by the large turbulent eddies resolved by LESs, since both Allen (1980) and Hugo (1989) are CAT-5 hurricanes, and Maria (2017) and Michael (2018) are CAT-3 hurricanes, the same as or similar to Isabel (2003) (CAT-5) simulated in this study. Fig. 6 compares the azimuthal-mean TKE and turbulent momentum fluxes as the function of the azimuthal-mean wind speeds quantified from the three "LES-100 runs" at the heights of 415–615 m with those derived from the fight measurements at the height level of ~500 m (adopted from Zhang et al., 2011a) and of ~600 m (adopted from Cione et al., 2020). The method used for calculating azimuthal-mean high-order turbulent moments from the LES output is presented in detail in section 3.4. As shown in Fig. 6, the magnitudes of the TKE and turbulent momentum fluxes quantified from the "LES runs" and their relationship to the mean wind speeds are overall consistent with the in-situ flight measurements. It should be noted that these five hurricanes are different storms after all, thus an apple-to-apple comparison is not possible. But the examination of the turbulent fluxes and TKE as the function of wind speeds should be a good way to compare the turbulent fields from different storms. The general consistency of the second-order turbulent moments between observations and simulations shown in Fig. 6 at least suggests that the LES generated turbulent fields in the eyewall are realistic.

The comparisons in storm intensity, mean R-Z structure of tangential wind and radial flow, vertical velocity structure, and turbulent kinetic moments between simulations and observations shown in Figs. 2–6 give us confidence that the LESs performed in this study can be used as the surrogate data to investigate the issues regarding the turbulent transport processes both within and above the boundary layer in the eyewall. In the following sections, we will present the simulated turbulent wind fields, the second-order moments, and their sensitivity to model horizontal grid spacing and 3D SGS models used in the simulations.

### 3.2. Turbulent velocity fields and large turbulent eddies

Previous studies show that the simulated TC intensity is sensitive to 1D PBL scheme used in convection permitting simulations (e.g., Nolan et al., 2009; Zhu et al., 2014). In this section, we examine the sensitivity of the simulated surface wind fields to the 3D SGS model and horizontal grid spacing in the LES setting in which the 1D PBL scheme is deactivated. Fig. 7a shows the time variation of the maximum 10-m wind speeds at model points from the seven experiments. The most striking feature is that the maximum wind speed from individual "LES-100 runs" can reach up to 110 $ms^{-1}$ (red, green, and blue dashed lines in Fig. 7a). In contrast, the wind speeds from the "PBL run" are only about 70 $ms^{-1}$ (black line in Fig. 7a). The wind speed difference between the "PBL run" and the mean over the six "LES runs" (thick grey line in Fig. 7a) reaches ~20 $ms^{-1}$ near the end of the simulations. The 10-m wind speeds averaged over the radii of 30–60 km (where the eyewall is located), however, tells a different story (Fig. 7b) where the "PBL run" produces the larger 10-m wind speeds (black line in Fig. 7b) than all "LES runs" by a larger margin. The different behaviors of the grid-point winds and mean winds over the eyewall between the "PBL run" and "LES runs" are caused by the wind gusts associated with the sub-kilometer and

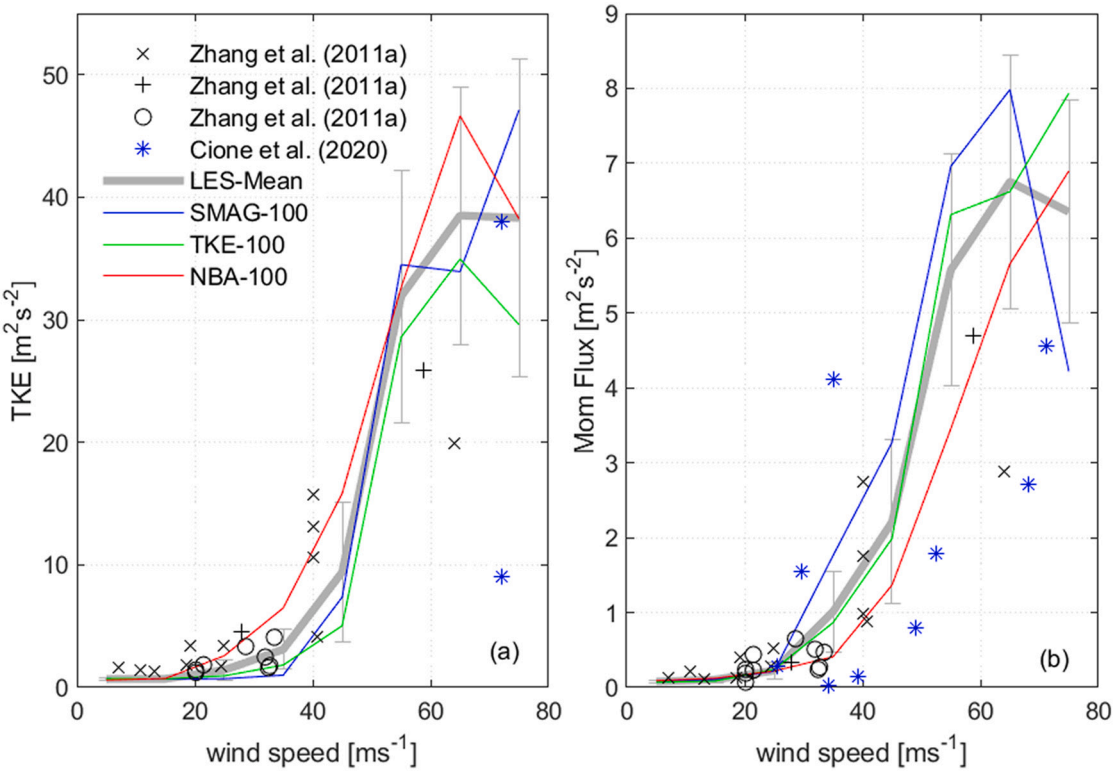


**Fig. 6.** Lines in (a) and (b) are the azimuthal-mean TKE and turbulent momentum fluxes as the function of azimuthal-mean wind speeds averaged over the heights of 415–615 m and period of 03–08 UTC, Sept. 12 from the three "LES-100 runs". The vertical bars indicate the standard deviation. Black ∘, +, and × indicate the TKE and turbulent momentum fluxes estimated from the aircraft measurements at the flight level of ~500 m height (after Fig. 9 of Zhang et al., 2011a). Blue * indicates the flight level data at ~600 m height from sUAS (after Figs. 7 and 8 of Coine et al. 2020). (For interpretation of the references to colour in this figure legend, the reader is referred to the web version of this article.)

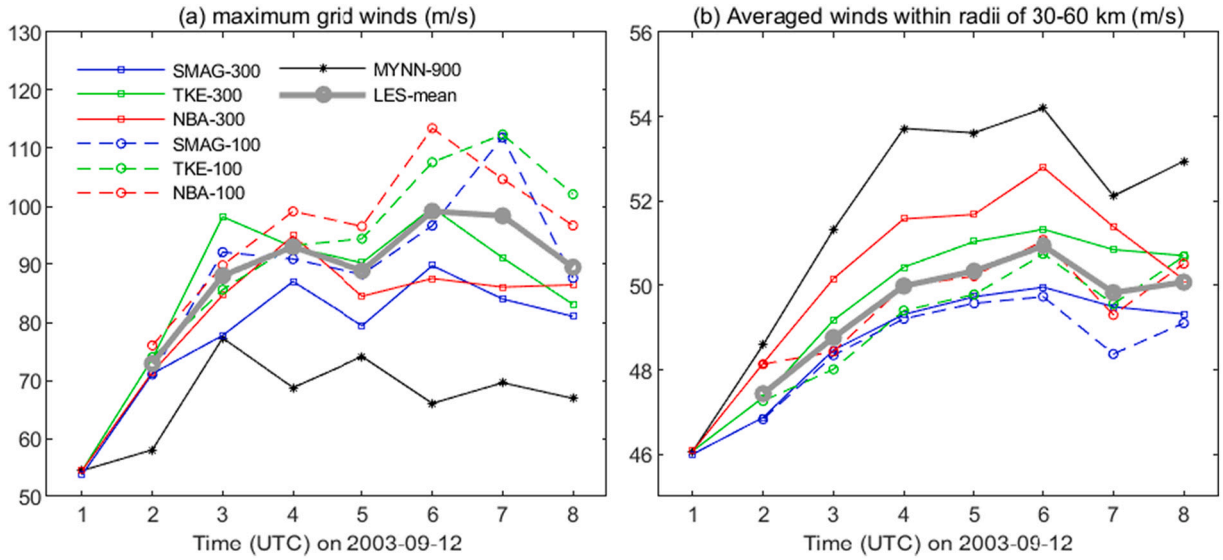


**Fig. 7.** Time series of (a) the maximum grid-point wind speed; and (b) the averaged wind speed over the radii between 30 and 60 km from the seven numerical experiments.

kilometer scale eddies resolved by LESs. Evidence of these large turbulent eddies and their skewed structure will be provided shortly.

In addition to the large difference of wind speeds between the "PBL run" and "LES runs", there are also inter-LES differences. All "LES-100 runs" produce the larger 10-m grid-point maximum wind speeds than the "LES-300 runs" (Fig. 7a). In contrast, the mean winds averaged over the eyewall from the "LES-300 runs" are consistently stronger than those in the "LES-100 runs", although the differences between them are not large, generally less than 2 $ms^{-1}$ with the largest and smallest differences shown in the NBA and SMAG runs, respectively (Fig. 7b). This phenomenon is similar to what is shown previously in Fig. 2 where the "LES-300 runs" produce the stronger 900-m re-gridded maximum surface wind speeds than the "LES-100 runs". This result is consistent with Green and Zhang (2015) who also showed that the 900-m re-gridded maximum surface wind speed is weaker in their NBA 100-m horizontal grid spacing run than that in the 300-m horizontal grid spacing run. We will show shortly that the cancellation between the wind maxima and minima associated with the downdrafts and updrafts of turbulent eddies is mainly responsible for generating the weaker re-gridded winds at 900-m horizontal grid spacing and mean winds over the eyewall in the "LES-100 runs".

To understand the interesting results shown in Figs. 2 and 7, it is helpful to look at the details of simulated surface wind fields. Fig. 8 shows the instantaneous 10-m horizontal wind speeds in the area of domain d05 at 03:00 UTC 12 September from the seven experiments. All simulations show that the strongest winds occur in the northwest quadrant of the vortex regardless of different model grid spacing and different methods for treating SGS turbulence, suggesting the robustness of the simulations in capturing vortex-scale features. A key difference between the "PBL run" and "LES runs" is the detailed wind features. In the MYNN-900 "PBL run", the wind distribution in the eyewall is fairly smooth and lacks fine-scale wind features. In contrast, eyewall disturbances with scales from several hundred meters to a few kilometers are seen in all "LES runs" at both 300 and 100 m horizontal grid spacing. These sub-kilometer and kilometer-scale eddies have been also reported in previous LES studies of TCs. For example, Rotunno et al. (2009) found that these 'vigorous small-scale eddies' are the dominant features in the eyewall in their LES run at the horizontal grid spacing of 62 m. Green and Zhang (2015) also showed such small-scale disturbances existing in all of their LES runs with the 3D NBA SGS model including the simulation at 333-m horizontal grid spacing.

Fig. 9 shows the instantaneous vertical velocity fields at 1 km altitude. Except for the "PBL run", all "LES runs" generate fine-scale up−/down-drafts in the eyewall. The dependence of eyewall disturbances on the model horizontal grid spacing and the SGS model is clearly shown in the figure. As expected, the eyewall up−/down-drafts in the "LES-100 runs" have finer scales than those in the "LES-300 runs". The eyewall disturbances generated by the NBA runs appear to have finer scales than those in the SMAG and TKE runs, particularly at the 300 m horizontal grid spacing. Such a sensitivity of eyewall disturbances to SGS models will be further discussed in the later sections.

The fine scale eyewall up−/down-draft couplets shown at 1 km altitude suggest that the secondary transverse circulations associated with the resolved large turbulent eddies are not shallow but connect the surface layer directly to the upper boundary layer via non-local mixing. Zhu (2008a) showed that the downdrafts of the secondary circulations are responsible for transporting momentum downward to result in the surface local wind maxima or gusts. This mechanism results in the large grid-point wind speeds in the "LES runs" shown in Fig. 7a. Wu et al. (2018) also reported that the local surface wind speeds may be doubled by the simulated large turbulent eddies including the tornado-scale vortices. In contrast to the downdrafts that generate local surface wind maxima, the updrafts of the eddy secondary circulations correspond to the local wind minima reflecting the air motion slowing down by the surface friction. To clearly show the difference of surface wind structure generated by the "PBL run" and "LES runs", we examined the distribution of the grid-point 10-m wind speeds in the seven experiments. Fig. 10 shows the percentage of wind speeds between 30 and 60 km in radii in the period of 03:00–08:00 UTC. Unlike the "PBL run", all "LES runs" produce long tails at the large wind end in the probability distribution consistent with the large grid-point wind speeds shown in Fig. 7a. However, since these peak winds only constitute a very small percentage of the wind speeds, they contribute little to the mean wind speed. The wind distribution of the MYNN-900 "PBL run", on the other hand, does not have a long tail at the high wind end, rather, a large percentage of winds falls in the range of 57–67 $ms^{-1}$. It is these winds that are mainly responsible for generating the larger mean wind speed over the eyewall of the MYNN-900 "PBL run" shown in Fig. 7b. In contrast, "LES runs" generate large percentages of winds in the ranges of 35–48 $ms^{-1}$. These smaller winds, which do not show in the "PBL run", are associated with the local wind minima induced by the large turbulent eddies and are the main cause for the smaller mean wind speeds over the eyewall of the "LES runs" shown in Fig. 7b. The long tails at the high wind end suggest that the large turbulent eddies resolved by LESs

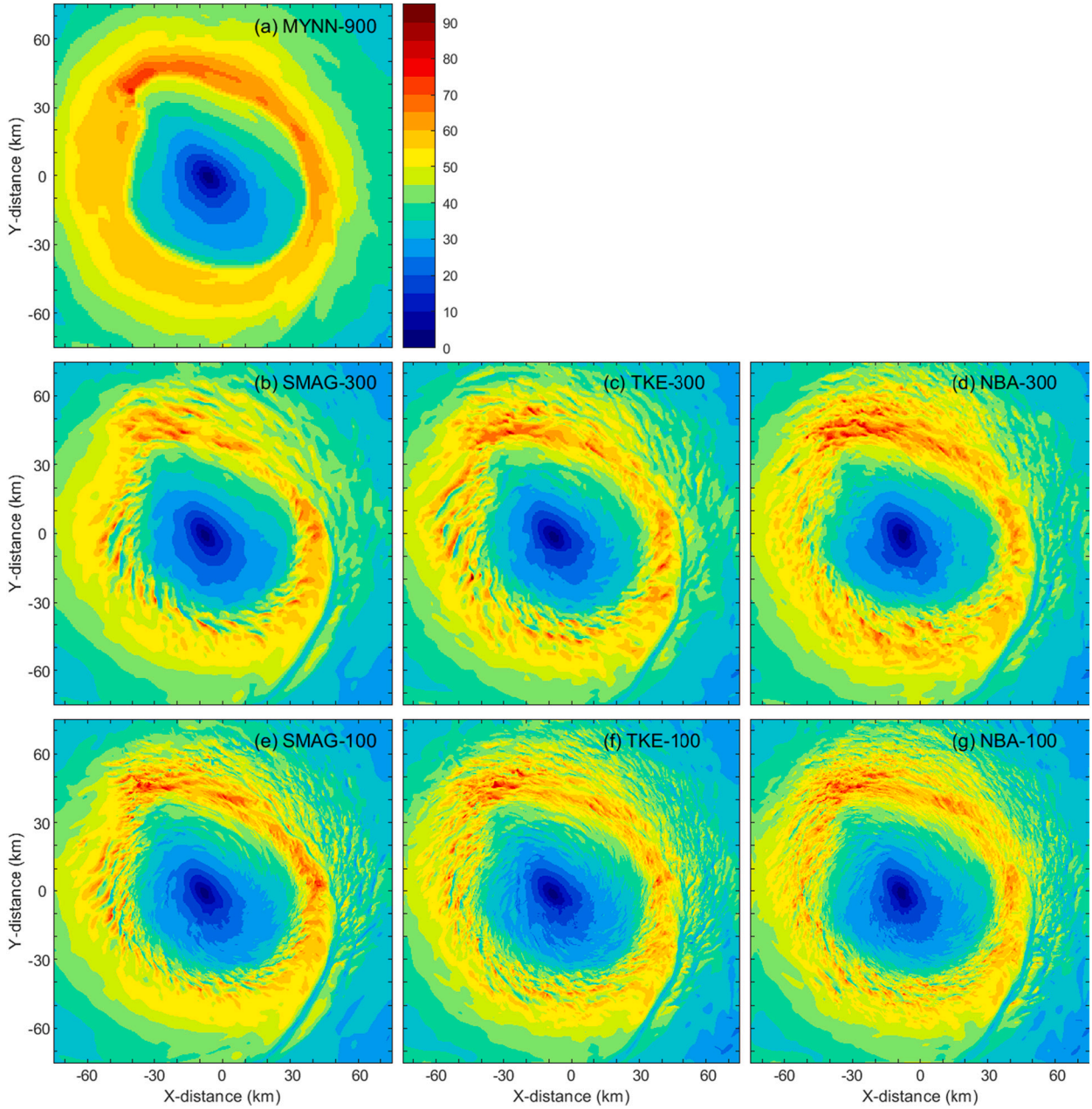


**Fig. 8.** Instantaneous 10-m wind speeds (m/ s) in the area of domain d05 at 03:00 UTC 12 September from the seven experiments.

have a skewed structure with narrow strong wind maxima and broad weak wind minima. This result is consistent with Zhu (2008a) who showed the skewed structure of large turbulent eddy circulations in the hurricane boundary layer. It is these skewed large turbulent eddies that cause the storm intensity in the "LES runs" to be greater than the best-track intensity (Fig. 2) since the latter is a measure of the storm's sustained wind speeds and the gust effect is not considered.

### *3.3. Impact of the parameterized SGS turbulent mixing on resolved eyewall disturbances*

To better understand the turbulent eddies resolved by LESs, we calculated turbulent eddy energy spectra using the model output. Fig. 11 shows the energy spectra of the vertical velocity of domain d05 at 500 m altitude from the seven experiments. Note that only the portion with wavelengths greater than 6 grid lengths are highlighted in the figure as the spectra at the smaller scales may not be reliable due to the 'unphysical' solutions caused by numerical diffusion (Bryan et al., 2003). The major characteristics of the calculated spectra including the range where the spectra follow the Kolmogorov power law are consistent with that of Green and Zhang (2015). The spectral peaks move to the shorter wavelengths as the model grid spacing decreases, which reflects well the scale change of the resolved eyewall disturbances shown in Figs. 8 and 9. Similar to Mirocha et al. (2010), the NBA runs somewhat produce more energetic smaller scale eddies and less energetic larger scale eddies than the SMAG runs, although the inter-LES differences are only marginal, particularly for the 100-m horizontal grid spacing runs.

In the convection permitting simulations in which the 1D PBL scheme is used to treat vertical turbulent mixing, Zhu et al. (2014) showed that the resolved fine-scale eyewall disturbances are sensitive to the parameterized vertical turbulent mixing. Small eddy exchange coefficients of vertical turbulent mixing tend to produce small-scale eyewall disturbances whereas large eddy exchange coefficients tend to

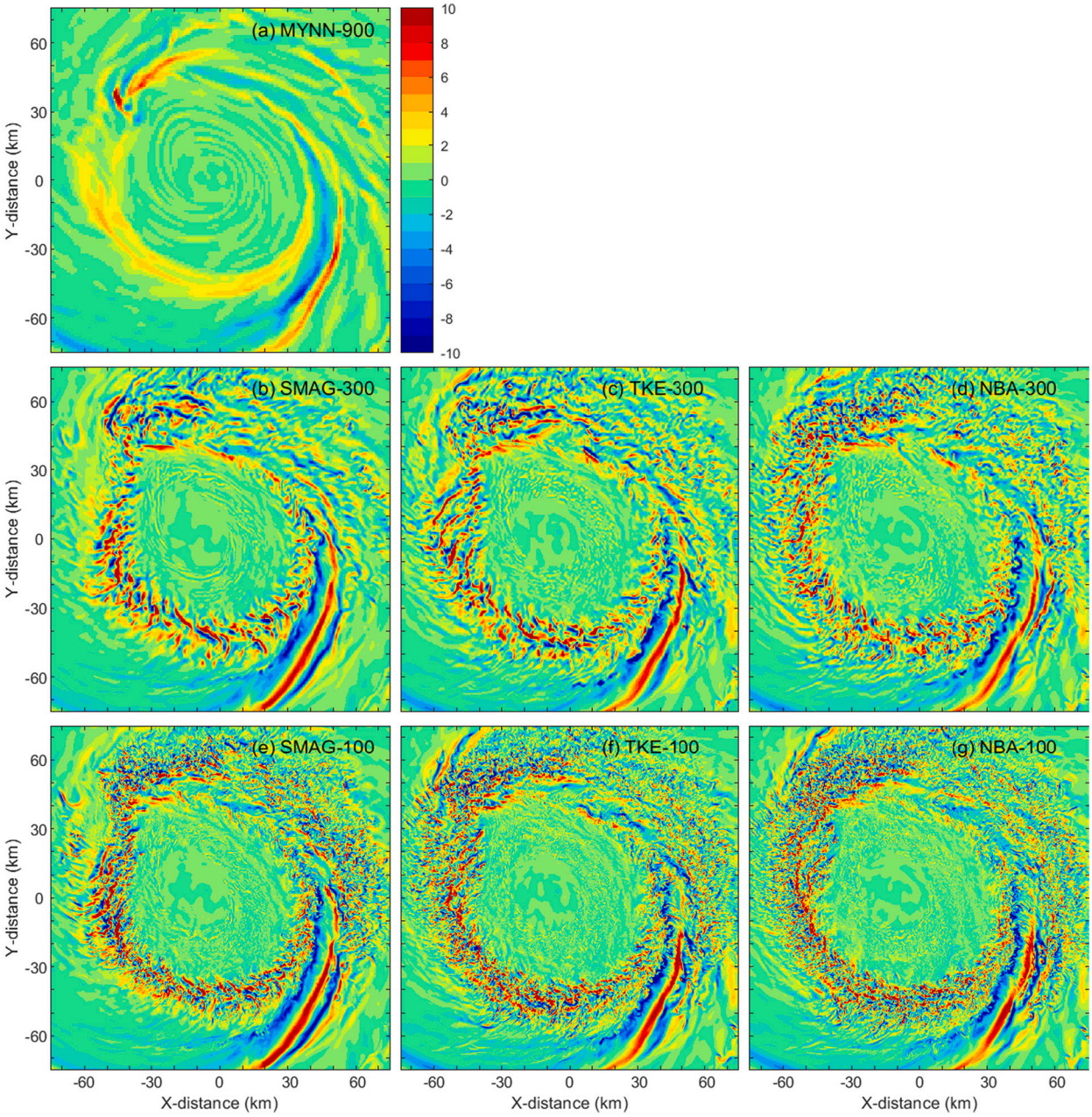


**Fig. 9.** 1000-m altitude vertical velocities ($ms^{-1}$) in the area of domain d05 at 03:00 UTC September 12 from the seven experiments.

organize the disturbances into eyewall mesovortices. To see if the resolved eyewall disturbances are modulated by the eddy exchange coefficients in the LES setting in which the 3D SGS model is used, we examined the SGS eddy exchange coefficients in the TKE and SMAG runs. Fig. 12 shows the R-Z structure of azimuthal-mean SGS horizontal and vertical eddy exchange coefficients from the SMAG-100 run and the vertical profiles of eddy exchange coefficients averaged over the radii of 30–60 km from both SMAG and TKE runs. Note that the NBA runs are not included in this comparison because the NBA SGS model uses a different approach to parameterize SGS turbulent transport. It calculates the SGS turbulent fluxes directly from the strain-rates or from the predicted SGS TKE, thus, no eddy exchange coefficient is needed in the NBA SGS model. Fig. 12 shows that at both horizontal grid spacing of 100 m and 300 m, the horizontal eddy exchange coefficients generated by the TKE and SMAG SGS models are similar, but the vertical eddy exchange coefficients generated by the TKE SGS model are much smaller than those generated by the SMAG SGS model above the boundary layer. Zhu et al. (2014) found that eyewall disturbances are sensitive to the vertical eddy exchange coefficients above the boundary layer since these small scale disturbances are not shallow flow features, and they extend well above the boundary layer. The fact that more energetic smaller scale eddies are generated in the TKE runs than those in the SMAG runs suggests that the finding by Zhu et al. (2014) obtained in the convection permitting simulations still holds for LESs, that is, smaller eddy exchange coefficients of vertical turbulent mixing tend to produce smaller scale eyewall disturbances.

To test the hypothesis that the eyewall disturbances can be modulated by the SGS eddy exchange coefficients in the LES setting, we performed four additional TKE-300 sensitive experiments in which the parameterized vertical and horizontal SGS eddy exchange coefficients are multiplied by a factor of 2 and 4. These sensitivity tests are named as TKE-300-V2, TKE-300-V4, TKE-300-H2, and TKE-300-H4, respectively. The vertical velocity spectra at 500 m altitude from these experiments are shown in Fig. 13. The decrease of spectral peak value and the shifting

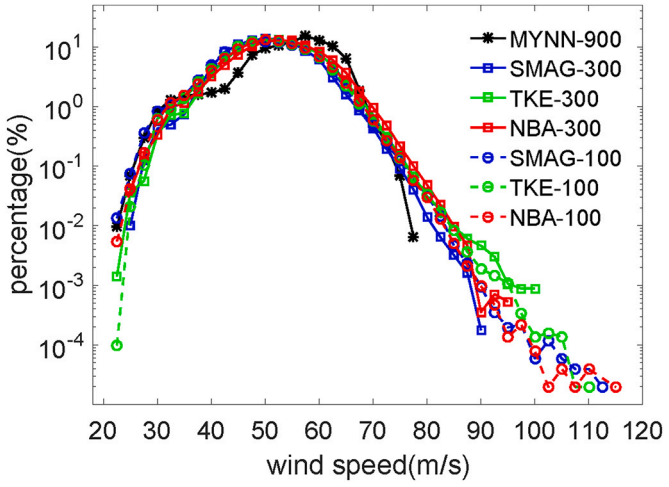


**Fig. 10.** Percentage of grid-point 10-m wind speeds between 30 and 60 km in radii in the period of 03:00–08:00 UTC Sept. 12 from the seven experiments.

of peak wavelength to larger scales in the sensitivity experiments imply that the energy-containing eddies shift to larger scales and become less energetic as the SGS eddy exchange coefficient increases. The figure also shows that the SGS vertical turbulent mixing (magenta solid and dashed lines in Fig. 13) tends to have a stronger impact on eyewall disturbances than the SGS horizontal turbulent mixing (cyan solid and dashed lines in Fig. 13). This result is consistent with what was found in convection permitting simulations (Zhu et al., 2014).

### 3.4. Eyewall vertical turbulent transport induced by the resolved eddies

In convection permitting simulations, large energy-containing eddies are not resolved. Their effects are parameterized by a 1D PBL scheme (or vertical turbulent mixing scheme). A key parameter in a PBL scheme is the eddy exchange coefficient from which the vertical turbulent fluxes are determined. In fair-weather conditions, the turbulent fluxes and the associated eddy exchange coefficients can be readily evaluated against the observations obtained in the boundary layer. In TC conditions, however, such an evaluation becomes a challenge because of the observational difficulties to obtain turbulent fluxes in violent convective conditions. To date, the vertical turbulent transport and the associated eddy exchange coefficients in the eyewall remain poorly characterized. LES is commonly considered as an approach that can realistically simulate large energy-containing eddies, but there are also issues of quantifying vertical turbulent fluxes from the LES output. One of the difficulties is how to appropriately define the mean of variables required for variance and covariance calculation. For fast responding in-situ observations, the mean is commonly defined as the average over a time period, and then, using the eddy correlation method to calculate the variance and covariance of variables. For the classic LES applications in non-TC conditions, the domain-mean is often used when calculating

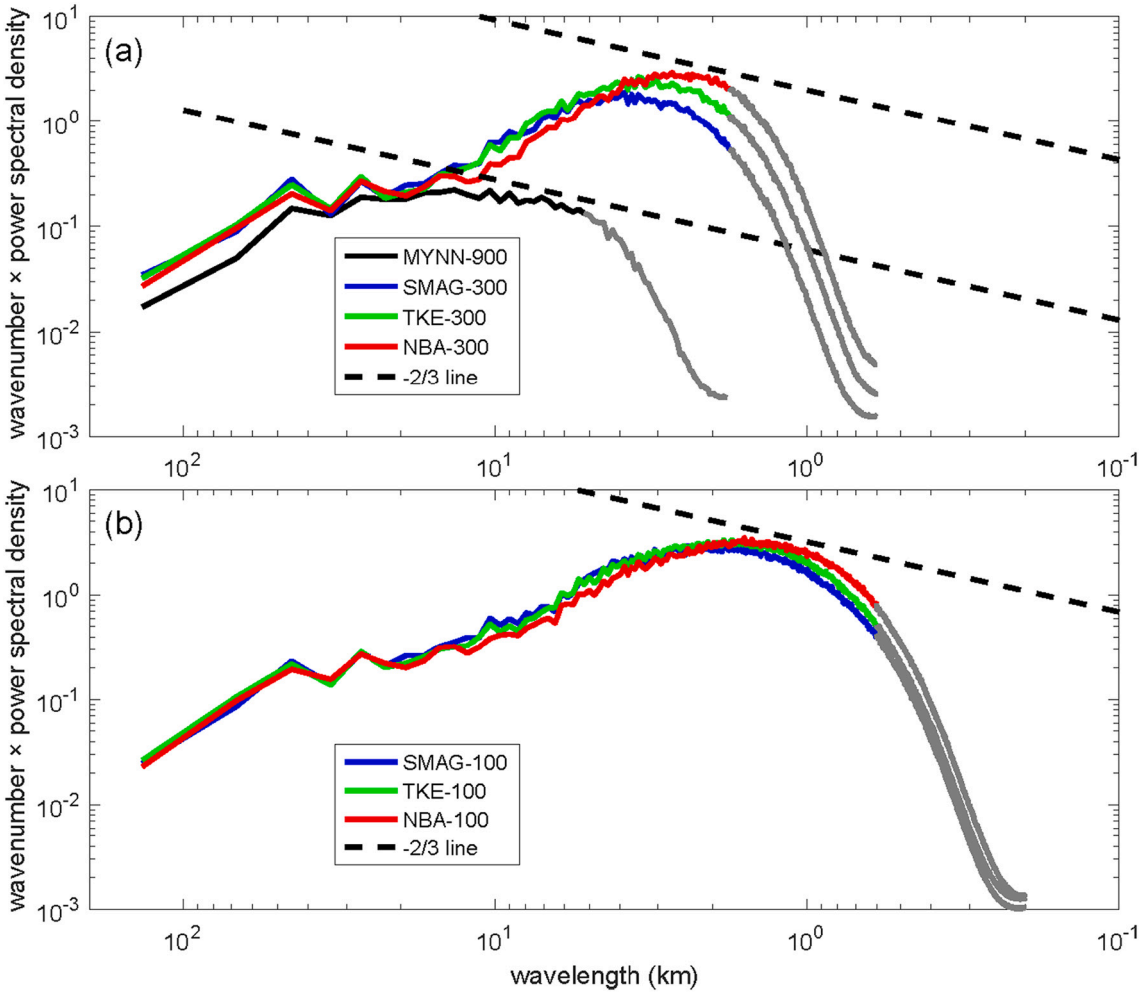


**Fig. 11.** Energy spectra of vertical velocities in domain d05 at 500 m altitude from the experiments of (a): MYNN-900, SMAG-300, TKE-300 and NBA-300; (b): SMAG-100, TKE-100 and NBA-100. The spectra have been averaged over the period from 03:00 UTC to 08:00 UTC, Sept. 12, 2003.

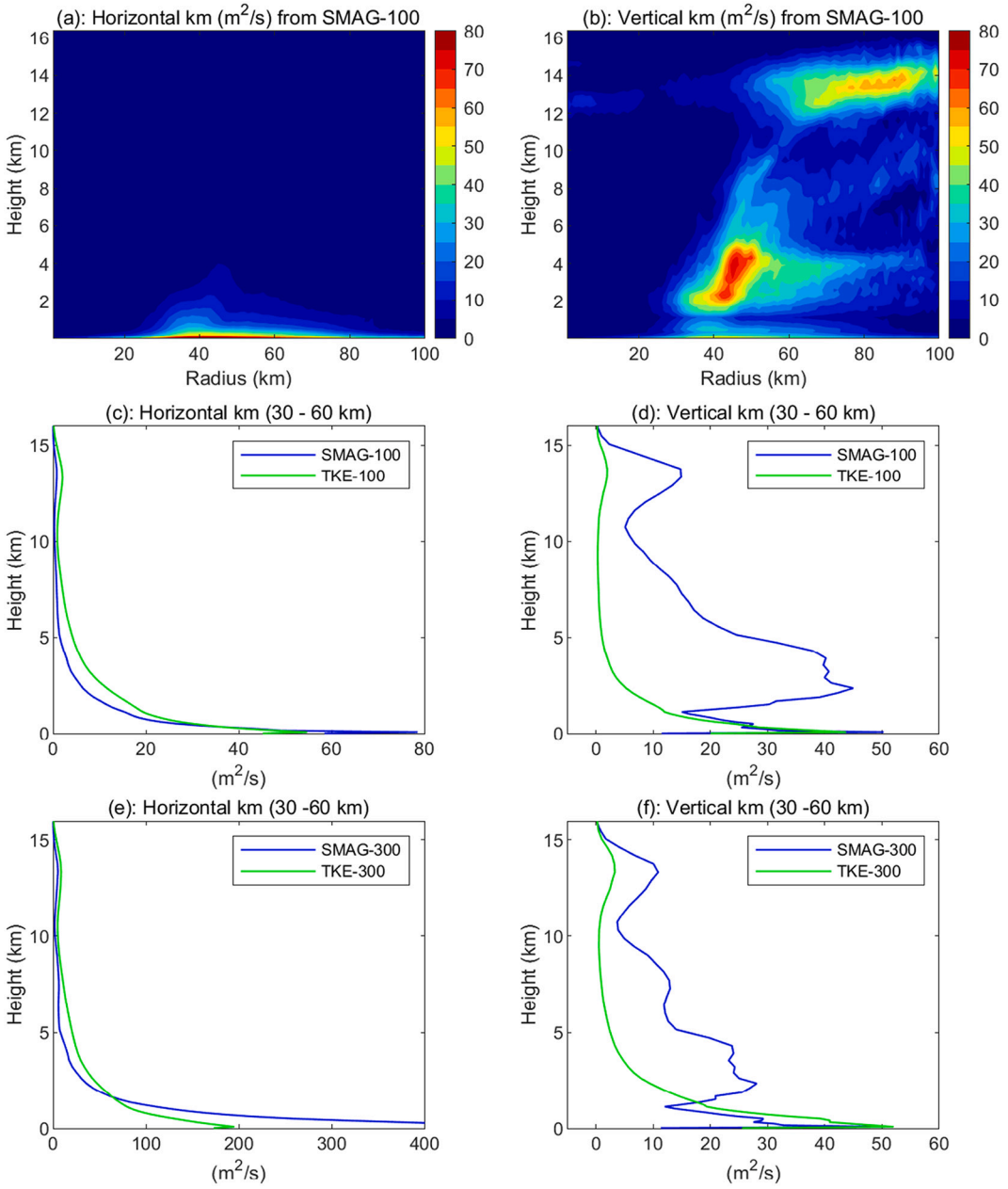


**Fig. 12.** (a) and (b): Azimuthal-mean radius-height distribution of horizontal and vertical SGS eddy exchange coefficients ($K_m$) from the SMAG-100 run, respectively. (c) and (d): Vertical profiles of horizontal and vertical km averaged over the radii of 30–60 km from the SMAG-100 and TKE-100 runs, respectively. (e) and (f): The same as (c) and (d) but for the SMAG-300 and TKE-300 runs. The results are averaged over the period from 03:00 UTC to 08:00 UTC.

high-order turbulent moments, which is appropriate as the ambient condition is often assumed to be horizontally homogeneous. However, the application of such a method to LESs of TCs becomes questionable since the fields of a storm vortex are not horizontally homogeneous. If an area for calculating the mean of variables would include both violent eyewall and peaceful eye, the estimated high-order turbulent moments would be exaggerated. Furthermore, if the eddy correlation method is applied to the entire LES domain, then, one would only obtain a single vertical profile of turbulent fluxes, eddy exchange coefficients, and other high-order turbulent moments. It would be incorrect to apply this vertical profile to both eyewall and eye of a storm since the turbulent mixing in these two regions is apparently different.

One way to solve this problem is to define a sub-domain centered at each model grid point, and then, use the LES output in the sub-domain for vertical flux calculation at each grid using the eddy correlation method via,

$$F_\varphi = \overline{w'\varphi'} = \overline{(w-\overline{w})(\varphi-\overline{\varphi})} \tag{1}$$

where $w$ is the vertical velocity, $\varphi$ is a generic scalar, $F_\varphi$ is the kinematic vertical flux of $\varphi$ at each grid point, overbar and prime indicate the mean over the sub-domain and the deviation away from the mean, respectively. In the first-order closure, the vertical momentum fluxes are assumed to be generated by the down-gradient diffusion processes and calculated as,

$$\overline{w'u'} = -K_m\frac{\partial\overline{u}}{\partial z}, \overline{w'v'} = -K_m\frac{\partial\overline{v}}{\partial z} \tag{2}$$

where $K_m$ is the eddy exchange coefficient of momentum, $\frac{\partial\overline{u}}{\partial z}$ and $\frac{\partial\overline{v}}{\partial z}$ are the vertical gradient of mean wind components over the sub-domain. In the eyewall, however, the non-local mixing induced by the convective

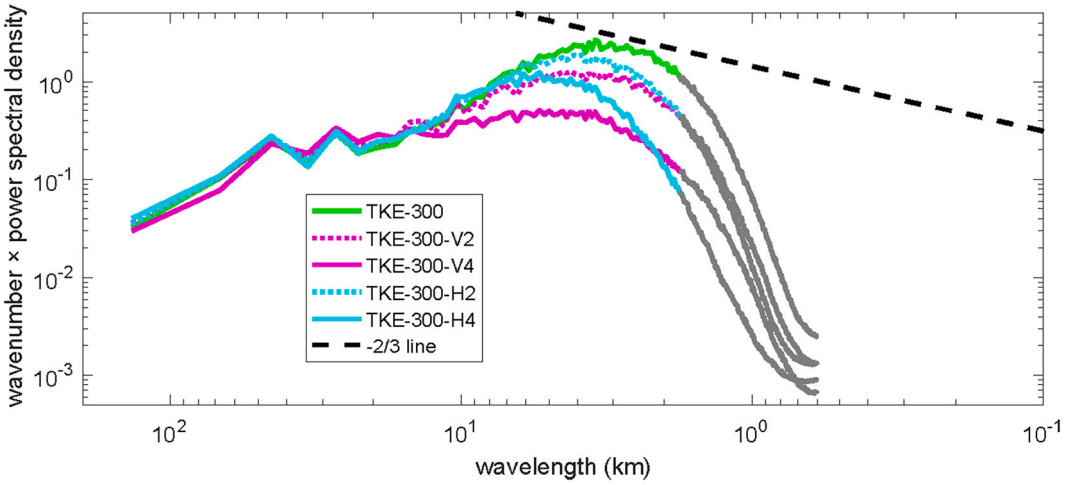


**Fig. 13.** Energy spectra of vertical velocities at 500 m altitude from the experiments of TKE-300, TKE-300-V2, TKE-300-V4, TKE-300-H2, and TKE-300-H4. The results have been averaged over the period from 03:00 UTC to 08:00 UTC Sept. 12, 2003.

cells (or eddies) generates a large amount of up-gradient vertical fluxes. Thus, to avoid the negative eddy exchange coefficients to be generated by Eq. (2), in this study, the momentum eddy exchange coefficient is calculated as,

$$K_m = \tau \Big/ \sqrt{\left(\frac{\partial \overline{u}}{\partial z}\right)^2 + \left(\frac{\partial \overline{v}}{\partial z}\right)^2} \tag{3}$$

where $\tau = (\overline{w'u'}^2 + \overline{w'v'}^2)^{\frac{1}{2}}$ is the total vertical momentum fluxes. A key question is how to define the size of a sub-domain for flux calculation using the eddy correlation method. The answer to the question does not depend on LES itself but on the grid resolution of a mesoscale model or a large-scale model to be evaluated by LES results. For example, if the grid spacing of a model is Δx, the minimum wavelength of eddies that can be resolved by this model will be 2Δx. Then, what needs to be parameterized in this model is the turbulent fluxes induced by eddies with wavelength smaller than 2Δx. In this case, a sub-domain of 2Δx by 2Δx from an LES would be appropriate to address the problem. As an illustration, Fig. 14 shows how a sub-domain at a grid point in an "LES-100 run" is defined for the flux calculation of this grid point. In this example, a sub-domain of 1.4 × 1.4 km$^2$ (containing 15 × 15 grid points) is defined for a grid point indicated by the green star. The model-resolved variables at these 15 × 15 grid points are used to calculate the fluxes at the grid point indicated by the green star using the eddy correlation method. As the green star runs over all the grid points in an LES domain, the fluxes of the entire TC vortex can be quantified. To calculate the vertical turbulent fluxes induced by eddies with different scales, we choose different sizes of sub-domains including 1 × 1 km$^2$, 2 × 2 km$^2$, 4 × 4 km$^2$, and 6 × 6 km$^2$. Once the model-resolved fluxes at each grid point is determined, the azimuthal-mean fluxes can be readily calculated by averaging over the rings from the storm center as the function of radii. Such a selection of sub-domains for flux calculation is based on two considerations. First, operational models now can have a grid spacing finer than 3 km owing to the ever-increasing computer technology. Thus, knowing turbulent fluxes induced by eddies with wavelength smaller than 6 km is the most desirable for parameterization development. Second, turbulence in the eyewall experiences a large radial gradient of mean fields across the eyewall. It remains unclear to what extent the large radial gradient can impact the structure of eddies, and how it will affect the fidelity of quantifying turbulent fluxes using eddy correlation method and estimating contributions of eddies with different scales to total fluxes. Presumably, eddies with larger scales will be affected more by the large radial gradient across the eyewall, thus, to mitigate the effect of possible sharp radial gradients across the eyewall

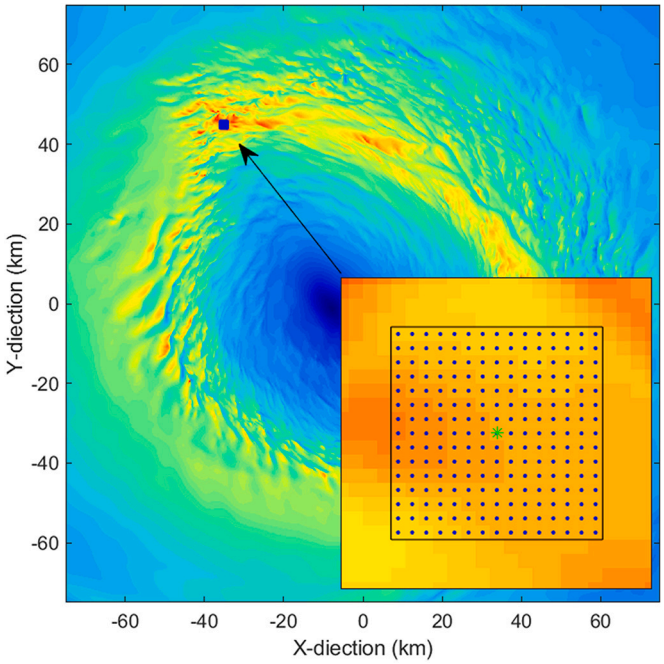


**Fig. 14.** Illustration of a sub-domain defined at a grid point for vertical flux calculation at the grid point using eddy correlation method.

on the flux calculation, we restrict the size of sub-domain to 6 × 6 km$^2$. Also as pointed out by Bryan et al. (2003), the sub-grid diffusion may have an effect on the simulated small scale eddies. This could introduce additional uncertainty in the flux calculation. Despite these possible uncertainties resulting from the large radial gradient across the eyewall and sub-grid diffusion, the flux calculation performed in this study should shed a light on the poorly understood vertical turbulent transport processes in the eyewall, particularly above the boundary layer.

Fig. 15 shows the azimuthal-mean R-Z structure of vertical momentum fluxes induced by the resolved eddies with different scales from the "TKE-100 run". Large vertical fluxes are seen in the eyewall. For eddies with scales smaller than 1 km (Fig. 15a), the peak of model-resolved momentum fluxes occurs in the boundary layer (~1 km depth following the conventional definition). This result is consistent with the typical boundary layer energetics that the peak energy spectrum occurs at a few hundreds of meters (Stull, 1988). Nonetheless,

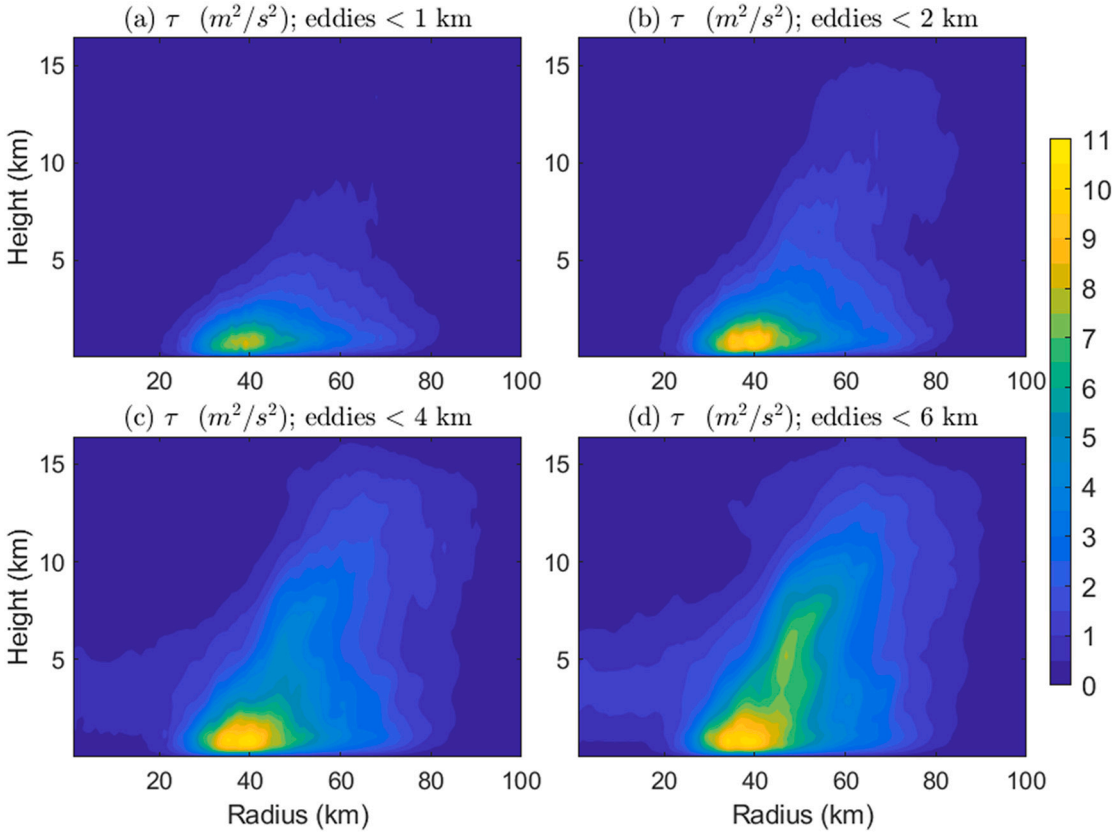


**Fig. 15.** Azimuthal-mean radius-height distribution of resolved vertical momentum fluxes $\tau = (\overline{w'u'}^2 + \overline{w'v'}^2)^{\frac{1}{2}}$ induced by eddies with different scales (a): smaller than 1 km; (b): smaller than 2 km; (c): smaller than 4 km; and (d): smaller than 6 km from the TKE-100 run. The results have been averaged over the period of 03:00–08:00 UTC Sept. 12, 2003.

there are non-negligible fluxes above the boundary layer in the eyewall, suggesting that sub-kilometer scale eddies also play a role in the vertical transport of momentum above the boundary layer in the eyewall. As large eddies greater than 1 km are included in the flux calculation, the model-resolved momentum fluxes increase substantially with the increase of height. A second peak of fluxes in the mid-troposphere around 5–7 km altitude starts to form when eddies with scales up to 6 km are included in the calculation (Fig. 15d). It suggests that large kilometer-scale eddies generated by the eyewall convection are the main contributors to the vertical momentum transport above the boundary layer in the eyewall.

To clearly demonstrate the individual contributions to the total momentum fluxes from the resolved eddies of different scales, Fig. 16 compares the vertical profiles of momentum fluxes associated with different size ranges of eddies averaged over the radii of 30–60 km from the three "LES-100 runs". The fluxes in a certain eddy range (e.g., 1–2 km) are calculated as the difference between the fluxes determined by the sub-domains of two different sizes (e.g., $1 \times 1$ km$^2$ and $2 \times 2$ km$^2$). Also shown in Fig. 16a are the SGS momentum fluxes determined by the 3D SGS models. There are interesting features shown in the figure. First, within the boundary layer (~1 km following the conventional definition), eddies with scales smaller than 1 km including SGS eddies are the main contributors to the vertical momentum transport. The contributions from larger eddies (> 1 km) to the momentum fluxes are minor and decrease substantially as the eddy scale increases. This result reflects the fact that large eddies are constrained by the surface friction so that kilometer-scale eddies are rare within the boundary layer. Second, above the boundary layer, large eddies with scales greater than 1 km become the main contributors to the vertical momentum transport. There is no flux discontinuity in the vertical to separate the turbulent transport generated by the surface turbulent processes and cloud turbulent processes aloft in the eyewall. There are large momentum fluxes above the boundary layer (dotted curves in Fig. 16a). This unique vertical structure of momentum transport in the eyewall is different from that in typical fair-weather conditions in which turbulent momentum fluxes mainly exist within the boundary layer. The decomposition of the fluxes in terms of eddy scales indicates that eddies with scales greater than 2 km are important to the vertical momentum transport in the eyewall. The peak values of momentum fluxes induced by eddies greater than 2 km occur in the mid-troposphere around 5–8 km (Fig. 16c–d). This result suggests that kilometer-scale eddies in the eyewall are the efficient momentum carriers, particularly above the boundary layer. Finally, the vertical profiles of resolved momentum fluxes obtained from the three "LES runs" are fairly consistent throughout the entire troposphere, suggesting that the momentum transport processes in the eyewall resolved by LESs are only marginally sensitive to the SGS models. This result gives us the confidence that the LESs performed in this study are robust and provide a useful dataset for understanding the turbulent transport processes in the eyewall.

It is important to keep in mind that part of the vertical fluxes induced by large eddies shown in Fig. 16 may be resolved in convection permitting simulations depending on the models' resolution. For example, if a mesoscale model has a grid spacing of 2 km, then, all fluxes induced by eddies greater than 2×2 km are explicitly resolved. What needs to be parameterized are those induced by eddies smaller than 2×2 km. The higher the model resolution, the more vertical fluxes will be resolved. However, even if the grid spacing of a model decreases to 1 km, as indicated by Fig. 16a, there is still an appreciable portion of fluxes induced by sub-kilometer eddies above the boundary layer in the eyewall. It remains to be a question if this portion of fluxes are important to TC evolution and if the PBL schemes used in models can appropriately parameterize the vertical fluxes induced by SGS eddies in the eyewall,

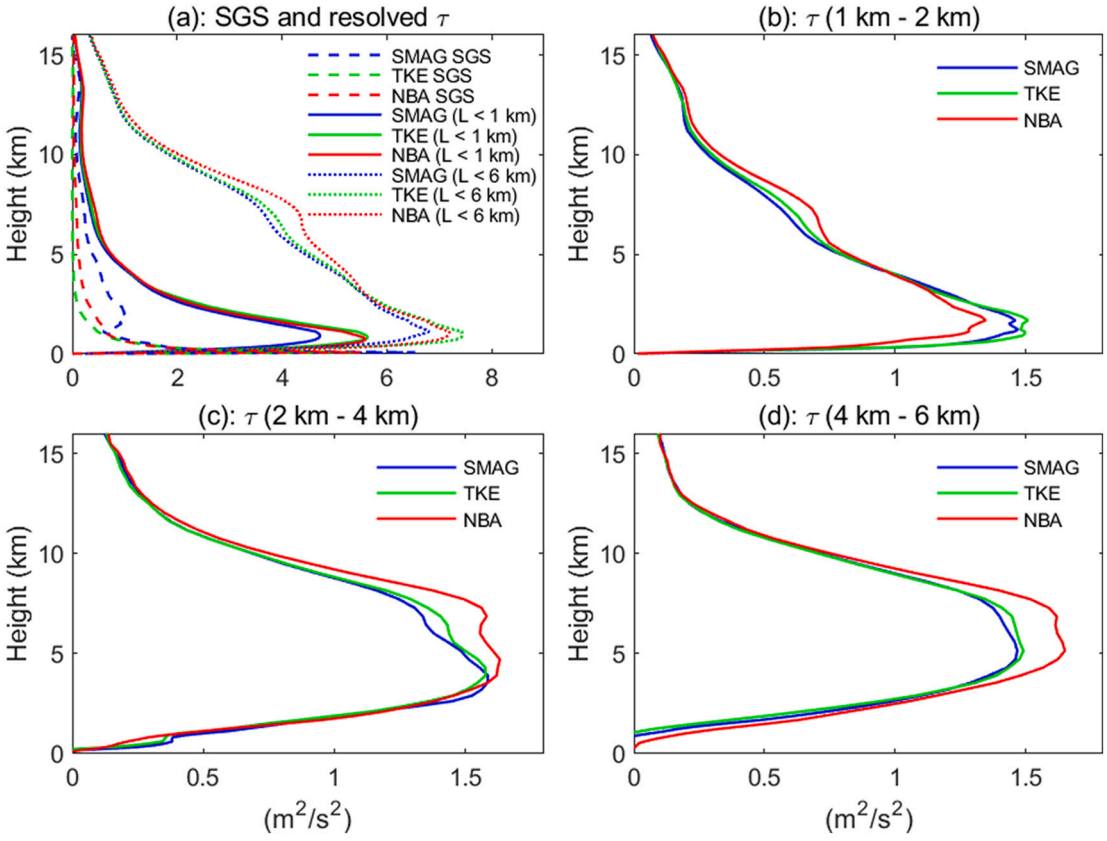


**Fig. 16.** Azimuthal-mean vertical momentum fluxes $\tau = (\overline{w'u'}^2 + \overline{w'v'}^2)^{\frac{1}{2}}$ induced by the resolved eddies with scales (a): ≤ 1 km and ≤ 6 km; (b): 1–2 km; (c): 2–4 km; and (d): 4–6 km from the three "LES-100 runs". The vertical profiles are averaged over the radii of 30–60 km and the period of 03:00–08:00 UTC. Also shown in (a) are the parameterized SGS momentum fluxes.

particularly those above the boundary layer.

Fig. 17 shows the vertical profiles of azimuthal-mean eddy exchange coefficients for momentum induced by eddies with different scales averaged over the radii of 30–60 km from the three "LES-100 runs". The consistent magnitude and vertical structure of eddy exchange coefficients from the three "LES runs" suggest that 100 m horizontal grid spacing appears to be sufficient for LESs to produce reliable turbulent processes in the eyewall. The results show that even for eddies with scales smaller than 1 km, the resultant $K_m$ does not become zero immediately above the boundary layer, but gradually decreases with height till mid-troposphere around 5 km altitude (solid curves in Fig. 17a). Larger eddies have a considerable contribution to $K_m$. When large eddies with scales up to 6 km are included in the calculation, it shows a nearly three-folder increase in the peak value of $K_m$ and the height of the peak $K_m$ moves from the top of the boundary layer up to approximately 4 km in altitude (dotted curves in Fig. 17a). The decomposition (Fig. 17b–d) shows that eddies with scales from 2 to 6 km have nearly equal contributions to the increase of $K_m$. Such an increase of $K_m$ may be explained by the representation of convectively driven non-local transport of large eddies in the eyewall using the down-gradient diffusion parameterization method. The combined effects of the large up-gradient vertical transport and small vertical gradient of mean winds lead to the large $K_m$. This is the notorious limitation of the first-order closure. The results shown in Fig. 17 indicate that the eddy exchange coefficient in the eyewall is scale-sensitive, particularly above the boundary layer. Such a strong dependence on eddy scales should be considered in the 1D PBL schemes used in the numerical models for TC prediction. It suggests that future improvements on 1D PBL schemes should focus on developing scale-aware eddy exchange coefficient formula so that the vertical turbulent transport in the eyewall can be appropriately parameterized.

## 4. Summary

This study aims to understand the numerically simulated wind structure and turbulent transport processes of a TC in the LES setting, namely, (a) the model grid resolution falls in the Kolmogorov inertial sub-range in turbulent energy spectra, and (b) 3D SGS models are used to treat horizontal and vertical SGS turbulent mixing. To do so, six LESs are performed to simulate Hurricane Isabel (2003). These include numerical simulations with two different horizontal spacing grids (300 m and 100 m) and three different 3D SGS models (3D SMAG, 3D TKE, and 3D NBA). The "LES runs" are further compared with a convection permitting simulation at a horizontal grid spacing of 900 m that uses a 1D PBL scheme (MYNN). The main results are summarized as follows.

The comparison between simulations and observations shows that the storm intensity, R-Z structure of tangential wind and radial flow, vertical velocity structure measured by CFAD, and TKE and turbulent momentum fluxes in the boundary layer simulated by the "LES runs" match well with the NHC best-track data, dropsonde composites, Doppler radar observations, and aircraft measurements. While all seven simulations produce fairly similar global R-Z structures of the mean TC vortex, there are noticeable differences between the "PBL run" and "LES runs". These include higher elevation of the peak tangential wind and deeper inflow layer in the "PBL run" than those in the "LES runs", suggesting the dependence of TC simulations on model horizontal grid spacing as well as the ways of treating horizontal and vertical SGS mixing. The inter-LES differences are generally smaller than that between the "PBL run" and "LES runs" and decrease with the increase of model horizontal grid resolution.

Unlike the "PBL run" that produces TC wind fields lacking small-scale perturbations, all "LES runs" produce kilometer and sub-kilometer eddy disturbances in the eyewall. The higher the model grid

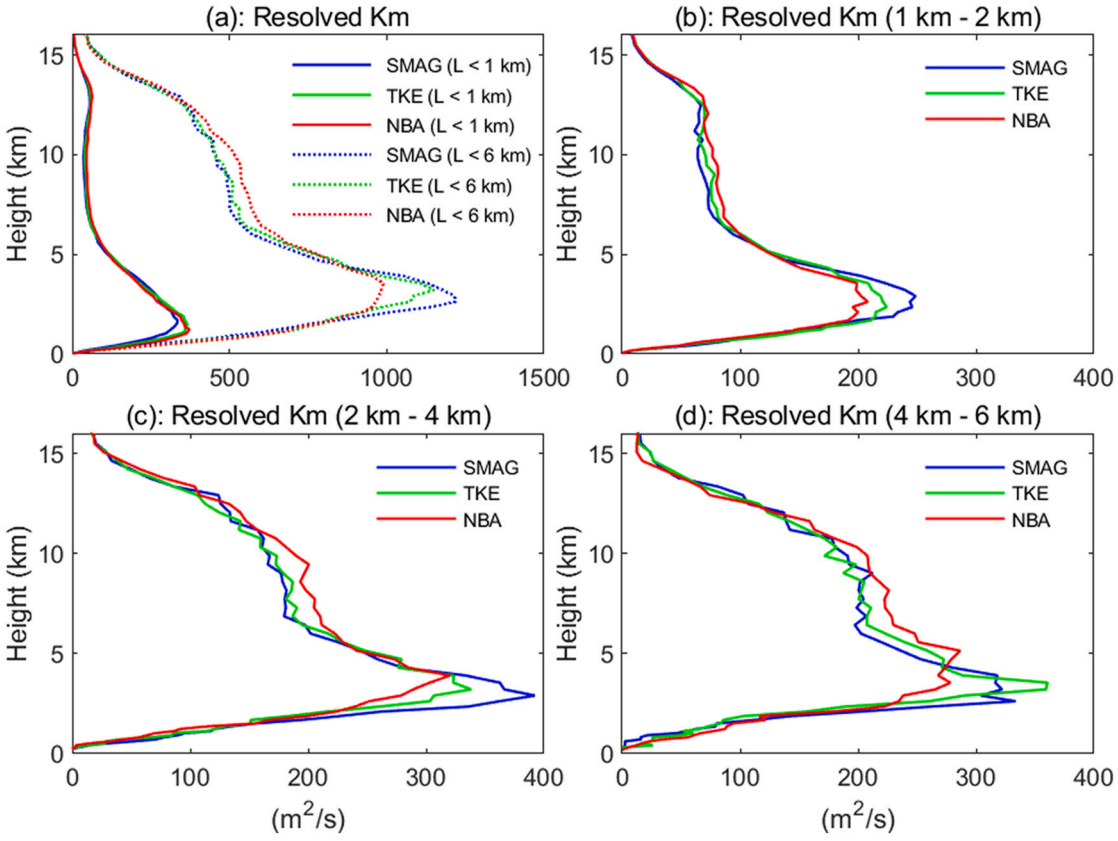


**Fig. 17.** Azimuthal-mean eddy momentum exchange coefficients $K_m$ induced by the resolved eddies with scales (a): ≤ 1 km and ≤ 6 km; (b): 1–2 km; (c): 2–4 km; and (d): 4–6 km from the three "LES-100 runs". The vertical profiles are averaged over the radii of 30–60 km and the period of 03:00–08:00 UTC.

resolution, the finer scale eddies are resolved. The eddy disturbances consist of overturning up−/down-draft couplets that are responsible for generating wind speed maxima and minima in the surface wind fields. As a result, the three "LES-100 runs" produce the peak surface grid-point wind speed up to 110 $ms^{-1}$, which is about 30 $ms^{-1}$ greater than that of the "PBL run". Even after re-gridding the winds to 900 m resolution (i.e., smoothing over a 900 m grid box), the mean surface wind speeds of all "LES runs" still exceed that of the "PBL run" by about 10 $ms^{-1}$. A detailed comparison shows that the re-gridded wind speeds of the "LES-300 runs" are greater than those of the "LES-100 runs". This result suggests that the peak grid-point wind speeds of 110 $ms^{-1}$ in the "LES-100 runs" are mainly produced by eddies with scales smaller than 300 m. Interestingly, the "PBL run" produces the greater mean surface wind speeds over the radii of 30–60 km than all "LES runs" by a margin up to 4 $ms^{-1}$. This is caused by the different eyewall disturbances generated in the two types of simulations ("PBL run" vs "LES run"). The "LES runs" generate a very skewed wind distribution with long tails at the high wind end. The small portion of peak wind maxima are smoothed out by the wind minima with a high percentage in the ranges of 35–48 $ms^{-1}$. In contrast, the "PBL run" generates a much less skewed wind distribution due to lack of kilometer and sub-kilometer eddies. The peak percentage of wind speed occurring in the range of 57–67 $ms^{-1}$ (which does not show in the "LES runs"), is mainly responsible for generating the larger mean wind speed in the eyewall than that of "LES runs". Similar to the azimuthal-mean R-Z wind structure, the inter-LES spread of surface winds decreases with the increase of model horizontal grid resolution. At 100-m horizontal grid spacing, the surface wind fields generated by the "LES runs" do not show significant sensitivity to different SGS models.

For a certain grid resolution, the scales of the eyewall eddy disturbances generated in the "LES runs" appear to be modulated by the SGS eddy exchange coefficients. Energy spectrum analyses show that large energy-containing eddies shift to larger scales and become less energetic as the SGS eddy exchange coefficients increase. Numerical experiments further indicate that the SGS vertical turbulent mixing tends to have a stronger impact on eyewall eddy disturbances than the SGS horizontal turbulent mixing. This result is consistent with what was found in convection permitting simulations in which a separate 1D PBL scheme outside the model dynamic core is used to parameterize eddy vertical mixing (Zhu et al., 2014).

Using the eddy correlation method, we examined second-order turbulent moments induced by the resolved eddies. At 100-m horizontal grid spacing, the vertical turbulent momentum fluxes induced by the resolved eddies do not appear to be substantially affected by the SGS models. All three LES-100 runs produce fairly consistent vertical profiles of resolved vertical momentum fluxes and associated eddy exchange coefficients in the eyewall. Such insensitivity of resolved turbulent transport in the eyewall to SGS mixing parameterization is consistent with the analyses of eddy energy spectra and wind distribution statistics shown in Figs. 10 and 11, suggesting that LES provides a reliable approach to investigate the turbulent transport processes in the inner-core region of a TC. A likely reason underlying such consistency in LESs at 100 m horizontal grid spacing is that the turbulence generated by the eyewall clouds above the boundary layer is far away from the surface boundaries. Unlike the turbulence within the boundary layer that is strongly affected by the surface, the free in-cloud turbulence is arguably easier to meet the basic assumptions of LESs. This question will be further investigated in our future studies.

Our calculations show that the vertical turbulent transport and the associated eddy exchange coefficients depend strongly on eddy scales. The vertical turbulent momentum fluxes induced by sub-kilometer eddies are mainly within the boundary layer (~ 1 km in depth) but also show a non-negligible portion above the boundary layer. Because of the constraint of the surface friction, large eddies with scales greater than 1 km are rare within the boundary layer, but start to increase above

the boundary layer and become the dominant contributors to the vertical momentum transport in the eyewall. The eddy exchange coefficients induced by the large eddies continue increasing with height and reach the peak in the mid-troposphere. This result suggests that the turbulent mixing within and above the boundary layer in the eyewall should be treated as a whole since there is no physical interface existing to separate the turbulence generated by the surface processes and cloud processes aloft. The decomposition of the fluxes in terms of eddy scales indicates that eddies with a spectrum of scales are all important to the vertical momentum transport in the eyewall. Kilometer-scale eddies are the efficient momentum carriers above the boundary layer. As a result, the total turbulent fluxes and the associated eddy exchange coefficients induced by eddies, say, with scales smaller than 4 km, are substantially larger than those induced by eddies with scales smaller than 2 km. This result has an important implication for future development and improvement of turbulent mixing parameterization in the eyewall. It suggests that vertical turbulent mixing parameterization in mesoscale simulations of TCs is ultimately a scale-sensitive problem. Future improvements on the PBL schemes should focus on developing scale-aware eddy exchange coefficient formula to reflect its sensitivity to model grid spacing so that the vertical turbulent transport within and above the boundary layer in the eyewall can be appropriately parameterized. Finally, we want to note two limitations of this study. First, the large radial gradient of mean fields across the eyewall may exert a non-negligible impact on eddy structures, and thus, there might be uncertainties associated with the turbulent flux estimation and the decomposition of fluxes in terms of eddy scales. How to appropriately quantify turbulent transport in the eyewall of a TC both observationally and numerically from LES output using eddy correlation method is an important issue that needs to be addressed. Second, due to the limited computing resources, the resolution of vertical grids above the boundary layer is configured low to accommodate the number of experiments performed in this study. It is unclear to what extent the low vertical resolution above the boundary layer will affect the fidelity of the simulated turbulent transport processes in the eyewall by LESs. These two issues will be tackled in our future research.

## Declaration of Competing Interest

The authors declare that they have no known competing financial interests or personal relationships that could have appeared to influence the work reported in this paper.

## Acknowledgments

The work is supported by the National Key Projects of the Ministry of Science and Technology of China (2018YFC1506405), National Natural Science Foundation of China (42075072, 41675009). the Innovation Group Project of Southern Marine Science and Engineering Guangdong Laboratory (Zhuhai) (311021008). Dr. Zhu wish to acknowledge his support by NOAA/HFIP under Grants NA14NWS4680030 and NA16NWS4680029, and National Science Foundation under Grant AGS-1822238. We are very grateful to the two anonymous reviewers for their constructive and insightful comments, which lead to the improvement of the paper. Data used in this study can be accessed at http://vortex.ihrc.fiu.edu/download/TC_LES/. The numerical calculations in this paper have been done on the supercomputing system in the Supercomputing Center of Nanjing University of Information Science & technology

## Appendix A. Appendix

The momentum governing equations used in the large-eddy simulations (LESs) may be written in Einstein summation convention as,

$$\frac{\partial \widetilde{u}_i}{\partial t}+\frac{\partial \widetilde{u}_i\widetilde{u}_j}{\partial x_j}+\epsilon_{ij3}f\widetilde{u}_i=-\frac{1}{\widetilde{\rho}}\frac{\partial \widetilde{p}}{\partial x_i}-g_i-\frac{\partial \tau_{ij}}{\partial x_j} \tag{A1}$$

where $\widetilde{u}_i$, $\widetilde{\rho}$, and $\widetilde{p}$ are the model-resolved velocities, density, and pressure, respectively; $f$ is the Coriolis parameter; $g_i=(0,0,g)$ is the gravity vector; and $\tau_{ij}$ is the sub-grid scale (SGS) stress.

For the 3D Smagorinsky and 3D TKE SGS models, $\tau_{ij}$ is parametrized as,

$$\tau_{ij}=-2K_m\widetilde{S}_{ij} \tag{A2}$$

where $\widetilde{S}_{ij}$ is the model-resolved strain-rate tensor represented as,

$$\widetilde{S}_{ij}=\frac{1}{2}\left(\frac{\partial \widetilde{u}_i}{\partial x_j}+\frac{\partial \widetilde{u}_j}{\partial x_i}\right) \tag{A3}$$

and $K_m$ is the 3D eddy exchange coefficient (or eddy diffusivity).

In the 3D Smagorinsky SGS model, $K_m$ is parameterized as,

$$K_m=(C_s l)^2\left[\max\left(0,\widetilde{S}_{ij}\widetilde{S}_{ij}-\mathrm{Pr}^{-1}N^2\right)\right]^{1/2} \tag{A4}$$

where $C_s$ is the Smagorinsky coefficient, which is 0.25 in WRF model, $l=(\Delta x\Delta y\Delta z)^{1/3}$ is the length scale and $Pr$ is the Prandtl number with a value of 0.7, while $N^2$ is the Brunt-Väisälä frequency.

In the 3D TKE SGS model, $K_m$ is parameterized as,

$$K_m=C_e l\sqrt{e} \tag{A5}$$

where $C_e=0.15$ is a coefficient and $e$ is the SGS TKE.

In the 3D NBA SGS model, SGS stress $\tau_{ij}$ is not determined via $K_m$ but calculated directly from either the model-resolved strain-rate tensor or SGS TKE as,

$$\tau_{ij} = -(C_s l)^2 \left[ 2\left( 2\widetilde{S}_{mn}\widetilde{S}_{mn} \right)^{\frac{1}{2}} \widetilde{S}_{ij} + C_1 \left( \widetilde{S}_{ik}\widetilde{S}_{kj} - \frac{1}{3}\widetilde{S}_{mn}\widetilde{S}_{mn}\delta_{ij} \right) + C_2 \left( \widetilde{S}_{ik}\widetilde{R}_{ik} - \widetilde{R}_{ik}\widetilde{S}_{kj} \right) \right] \tag{A6}$$

$$\tau_{ij} = -C_e l \left\{ 2e^{\frac{1}{2}}\widetilde{S}_{ij} + \left( \frac{27}{8\pi} \right)^{\frac{1}{3}} C_S^{\frac{2}{3}} l \left[ C_1 \left( \widetilde{S}_{ik}\widetilde{S}_{kj} - \frac{1}{3}\widetilde{S}_{mn}\widetilde{S}_{mn}\delta_{ij} \right) + C_2 \left( \widetilde{S}_{ik}\widetilde{R}_{ik} - \widetilde{R}_{ik}\widetilde{S}_{kj} \right) \right] \right\} \tag{A7}$$

where $\widetilde{R}_{ij}$ is the model-resolved rotation-rate tensor represented as,

$$\widetilde{R}_{ij} = \frac{1}{2}\left( \frac{\partial \widetilde{u}_i}{\partial x_j} - \frac{\partial \widetilde{u}_j}{\partial x_i} \right) \tag{A8}$$

and $C_e = [8\pi/27]^{1/3} C_S{}^{4/3}$, $C_1 = C_2 = 960^{\frac{1}{2}} C_b/7(1+C_b)S_k$, $S_k = 0.5$. $C_b = 0.36$ is the backscatter parameter defined as the ratio of the rate of backscatter of TKE to the dissipation rate. While the second and third high terms on the right-hand side of Eq. (A7) represent the backscatter and normal stresses in the sheared turbulence. In this study, we use the TKE option since it is more suitable to account for the buoyancy production of turbulence in the eyewall and rainbands.

Once $K_m$ is determined, the eddy exchange coefficient for scalar variables, such as heat and moisture, is parameterized as,

$$K_h = \left( 1 + \frac{2l_v}{\Delta z} \right) K_m \tag{A9}$$

while $l_v$ is the vertical length scale taken as,

$$l_v = \begin{cases} \Delta z \ (\textit{neutral or unstable stratification}) \\ min(\Delta z, l_s) \ (\text{stable stratification}) \end{cases} \tag{A10}$$

and $l_s$ is a length scale relates to the stability as,

$$l_s = 0.76 e^{1/2} \left| \frac{g}{\widetilde{\theta}_v} \frac{\partial \widetilde{\theta}_v}{\partial z} \right|^{-1/2} \tag{A11}$$

where $\widetilde{\theta}_v$ is the model-resolved virtual potential temperature. Note that the NBA scheme only corrects the SGS stress $\tau_{ij}$ calculation. In WRF simulations, it is activated in conjunction with either the Smagorinsky scheme or TKE scheme. It overwrites the SGS stress $\tau_{ij}$ determined by the Smagorinsky scheme or TKE scheme depending on which scheme is activated but retains the heat and moisture fluxes determined by the scheme. In our simulations, the NBA scheme is used with the TKE scheme, therefore, the SGS heat and moisture fluxes in the NBA scheme are calculated the same as those in the TKE scheme.

## References


Aberson, S., Montgomery, M.T., Bell, M.M., Black, M., 2006. Hurricane Isabel (2003): new insights into the physics of intense storms. Part II: extreme localized wind. Bull. Am. Meteorol. Soc. 87, 1349–1354.

Bao, J.W., Gopalakrishnan, S.G., Michelson, S.A., Marks, F.D., Montgomery, M.T., 2012. Impact of physics representations in the HWRFX on simulated hurricane structure and pressure–wind relationships. Mon. Weather Rev. 140 (10), 3278–3299.

Beljaars, A.C., 1995. The parametrization of surface fluxes in large-scale models under free convection. Q. J. R. Meteorol. Soc. 121 (522), 255–270.

Black, P.G., D'Asaro, E.A., Drennan, W.M., French, J.R., Niiler, P.P., Sanford, T.B., Terrill, E.J., Walsh, E.J., Zhang, J.A., 2007. Air–sea exchange in hurricanes: synthesis of observations from the coupled boundary layer air–sea transfer experiment. Bull. Am. Meteor. Soc. 88, 357–374.

Bryan, G.H., 2012. Effects of surface exchange coefficients and turbulence length scales on the intensity and structure of numerically simulated hurricanes. Mon. Weather Rev. 140 (4), 1125–1143.

Bryan, G.H., Rotunno, R., 2009. The maximum intensity of tropical cyclones in axisymmetric numerical model simulations. Mon. Weather Rev. 137 (6), 1770–1789.

Bryan, G.H., Wyngaard, J.C., Fritsch, J.M., 2003. Resolution requirements for the simulation of deep moist convection. Mon. Weather Rev. 131 (10), 2394–2416.

Cione, J.J., Bryan, G.H., Dobosy, R., Zhang, J.A., de Boer, G., Aksoy, A., Wadler, J.B., Kalina, E.A., Dahl, B.A., Ryan, K., Neuhaus, J., 2020. Eye of the storm: observing hurricanes with a small unmanned aircraft system. Bull. Am. Meteorol. Soc. 101 (2), E186–E205.

Deardorff, J.W., 1970. A numerical study of three-dimensional turbulent channel flow at large Reynolds numbers. J. Fluid Mech. 41 (2), 453–480.

Deardorff, J.W., 1980. Stratocumulus-capped mixed layers derived from a three-dimensional model. Bound.-Layer Meteorol. 18 (4), 495–527.

Donelan, M.A., Haus, B.K., Reul, N., Plant, W.J., Stiassnie, M., Graber, H.C., Brown, O.B., Saltzman, E.S., 2004. On the limiting aerodynamic roughness of the ocean in very strong winds. Geophys. Res. Lett. 31 (18), L18306.

Drennan, W.M., Zhang, J.A., French, J.R., McCormick, C., Black, P.G., 2007. Turbulent fluxes in the hurricane boundary layer. Part II. Latent heat fluxes. J. Atmos. Sci. 64, 1103–1115.

Dudhia, J., 1989. Numerical study of convection observed during the winter monsoon experiment using a mesoscale two-dimensional model. J. Atmos. Sci. 46 (20), 3077–3107.

Dudhia, J., 1996. A multi-layer soil temperature model for MM5. In Preprints. In: The Sixth PSU/NCAR Mesoscale Model Users' Workshop, pp. 22–24.

French, J.R., Drennan, W.M., Zhang, J.A., Black, P.G., 2007. Turbulent fluxes in the hurricane boundary layer. Part I: momentum flux. J. Atmos. Sci. 64, 1089–1102.

Gamache, J.F., 1997. Evaluation of a fully three-dimensional variational Doppler analysis technique. Preprints. In: 28th Conf. on Radar Meteorology, Austin, TX. Amer. Meteor. Soc, pp. 422–423.

Gamache, J.F., Marks, F.D., Roux, F., 1995. Comparison of three airborne Doppler sampling techniques with airborne in-situ wind observations in Hurricane Gustav (1990). J. Atmos. Ocean. Technol. 12, 171–181.

Garratt, J.R., 1992. The Atmospheric Boundary Layer. Cambridge University Press, 316 pp.

Gopalakrishnan, S.G., Marks Jr., F., Zhang, J.A., Zhang, X., Bao, J.W., Tallapragada, V., 2013. A study of the impacts of vertical diffusion on the structure and intensity of the tropical cyclones using the high-resolution HWRF system. J. Atmos. Sci. 70 (2), 524–541.

Green, B.W., Zhang, F., 2015. Numerical simulations of Hurricane Katrina (2005) in the turbulent gray zone. J. Adv. Model. Earth Syst. 7 (1), 142–161.

Hence, D.A., Houze Jr., R.A., 2008. Kinematic structure of convective-scale elements in the rainbands of Hurricanes Katrina and Rita (2005). J. Geophys. Res. 113, D15108 https://doi.org/10.1029/2007JD009429.

Kain, J.S., Fritsch, J.M., 1993. Convective parameterization for mesoscale models: the Kain-Fritsch scheme. In: The Representation of Cumulus Convection in Numerical Models. American Meteorological Society, Boston, MA, pp. 165–170.

Kepert, J.D., 2012. Choosing a boundary layer parameterization for tropical cyclone modeling. Mon. Weather Rev. 140 (5), 1427–1445.

Kolmogorov, A.N., 1941. The local structure of turbulence in incompressible viscous fluid for very large Reynolds numbers. Cr Acad. Sci. URSS 30, 301–305.
Kosović, B., 1997. Subgrid-scale modelling for the large-eddy simulation of high-Reynolds-number boundary layers. J. Fluid Mech. 336, 151–182.
Li, X., Pu, Z., 2008. Sensitivity of numerical simulation of early rapid intensification of Hurricane Emily (2005) to cloud microphysical and planetary boundary layer parameterizations. Mon. Weather Rev. 136 (12), 4819–4838.
Li, X., Pu, Z., 2021. Vertical eddy diffusivity parameterization based on a large-eddy simulation and its impact on prediction of hurricane landfall. Geophys. Res. Lett. 48 https://doi.org/10.1029/2020GL090703 e2020GL090703.
Lilly, D.K., 1967. The representation of small-scale turbulence in numerical experiment. In: Proc. IBM Scientific Computing Symp. on Environmental Sciences, White Plains, NY. IBM, pp. 195–210.
Lorsolo, S., Zhang, J.A., Marks Jr., F., Gamache, J., 2010. Estimation and mapping of hurricane turbulent energy using airborne Doppler measurements. Mon. Weather Rev. 138 (9), 3656–3670.
Lundquist, J.K., Chan, S.T., 2007. Consequences of urban stability conditions for computational fluid dynamics simulations of urban dispersion. J. Appl. Meteorol. Climatol. 46 (7), 1080–1097.
MacVean, M.K., Mason, P.J., 1990. Cloud-top entrainment instability through small-scale mixing and its parameterization in numerical models. J. Atmos. Sci. 47 (8), 1012–1030.
Marks, F.D., Black, P.G., Montgomery, M.T., Burpee, R.W., 2008. Structure of the eye and eyewall of Hurricane Hugo (1989). Mon. Weather Rev. 136, 1237–1259.
Mason, P.J., Thomson, D.J., 1992. Stochastic backscatter in large-eddy simulations of boundary layers. J. Fluid Mech. 242, 51–78.
Mirocha, J.D., Lundquist, J.K., Kosović, B., 2010. Implementation of a nonlinear subfilter turbulence stress model for large-eddy simulation in the Advanced Research WRF model. Mon. Weather Rev. 138 (11), 4212–4228.
Mlawer, E.J., Taubman, S.J., Brown, P.D., Iacono, M.J., Clough, S.A., 1997. Radiative transfer for inhomogeneous atmospheres: RRTM, a validated correlated-k model for the longwave. J. Geophys. Res.-Atmos. 102 (D14), 16663–16682.
Nakanishi, M., Niino, H., 2004. An improved Mellor–Yamada level-3 model with condensation physics: its design and verification. Bound.-Layer Meteorol. 112 (1), 1–31.
Nolan, D.S., Zhang, J.A., Stern, D.P., 2009. Evaluation of planetary boundary layer parameterizations in tropical cyclones by comparison of in situ observations and high-resolution simulations of Hurricane Isabel (2003). Part I: Initialization, maximum winds, and the outer-core boundary layer. Mon. Weather Rev. 137 (11), 3651–3674.
Reasor, P.D., Rogers, R., Lorsolo, S., 2013. Environmental flow impacts on tropical cyclone structure diagnosed from airborne doppler radar composites. Mon. Weather Rev. 141, 2949–2969.
Rogers, R., Reasor, P., 2013. Airborne doppler observations of the inner-core structural differences between intensifying and steady-state tropical cyclones. Mon. Weather Rev. 141, 2970–2991.
Rotunno, R., Chen, Y., Wang, W., Davis, C., Dudhia, J., Holland, G.J., 2009. Large-eddy simulation of an idealized tropical cyclone. Bull. Am. Meteorol. Soc. 90 (12), 1783–1788.
Skamarock, W.C., Klemp, J.B., Dudhia, J., Gill, D.O., Barker, D.M., Duda, M.G., Huang, X. Y., Wang, W., Powers, J.G., 2008. A Description of the Advanced Research WRF Version 3. NCAR Technical Note. National Center for Atmospheric Research, Boulder, CO, USA.
Smagorinsky, J., 1963. General circulation experiments with the primitive equations: I. the basic experiment. Mon. Weather Rev. 91 (3), 99–164.
Stevens, B., Moeng, C.H., Ackerman, A.S., Bretherton, C.S., Chlond, A., de Roode, S., Edwards, J., Golaz, J.C., Jiang, H., Khairoutdinov, M., Kirkpatrick, M.P., Lewellen, D.C., Lock, A., Muller, F., Stevens, D.E., Whelan, E., Zhu, P., 2005. Evaluation of large-eddy simulations via observations of nocturnal marine stratocumulus. Mon. Weather Rev. 133 (6), 1443–1462.
Stull, R.B., 1988. An Introduction to Boundary Layer Meteorology. Atmospheric Sciences Library. Kluwer, Dordrecht, p. 1988.
Thompson, G., Field, P.R., Rasmussen, R.M., Hall, W.D., 2008. Explicit forecasts of winter precipitation using an improved bulk microphysics scheme. Part II: Implementation of a new snow parameterization. Mon. Weather Rev. 136 (12), 5095–5115.
Wu, L., Liu, Q., Li, Y., 2018. Prevalence of tornado-scale vortices in the tropical cyclone eyewall. Proc. Natl. Acad. Sci. 115 (33), 8307–8310.
Yuter, S.E., Houze, R.A., 1995. Three-dimensional kinematic and microphysical evolution of Florida cumulonimbus. Part II: frequency distributions of vertical velocity, reflectivity, and differential reflectivity. Mon. Weather Rev. 123, 1941–1963.
Zhang, D., Anthes, R.A., 1982. A high-resolution model of the planetary boundary layer—Sensitivity tests and comparisons with SESAME-79 data. J. Appl. Meteorol. 21 (11), 1594–1609.
Zhang, F., Pu, Z., 2017. Effects of vertical eddy diffusivity parameterization on the evolution of landfalling hurricanes. J. Atmos. Sci. 74, 879–1905.
Zhang, J.A., Black, P.G., French, J.R., Drennan, W.M., 2008. First direct measurements of enthalpy flux in the hurricane boundary layer: the CBLAST results. Geophys. Res. Lett. 35, L14813 https://doi.org/10.1029/2008GL034374.
Zhang, J.A., Marks, F.D., Montgomery, M.T., Lorsolo, S., 2011a. An estimation of turbulent characteristics in the low-level region of intense hurricanes Allen (1980) and Hugo (1989). Mon. Weather Rev. 139, 1447–1462.
Zhang, J.A., Rogers, R.F., Nolan, D.S., Marks, F.D., 2011b. On the characteristic height scales of the Hurricane boundary layer. Mon. Weather Rev. 139, 2523–2535.
Zhang, J.A., Rogers, R., Marks, F.D., Tallapragada, V., 2018. Evaluating the impact of parameterized turbulent mixing and boundary layer structure on hurricane intensification. In: 23 Symposium on Boundary Layers and Turbulence.
Zhang, J.A., Kalina, E.A., Biswas, M.K., Rogers, R.F., Zhu, P., Marks, F.D., 2020. A review and evaluation of planetary boundary layer parameterizations in hurricane weather research and forecasting model using idealized simulations and observations. Atmosphere 11 (10), 1091. https://doi.org/10.3390/atmos11101091.
Zhu, P., 2008a. Simulation and parameterization of the turbulent transport in the hurricane boundary layer by large eddies. J. Geophys. Res.-Atmos. 113, D17104.
Zhu, P., 2008b. Impact of land-surface roughness on surface winds during hurricane landfall. Q. J. R. Meteorol. Soc. 134 (633), 1051–1057.
Zhu, P., Menelaou, K., Zhu, Z., 2014. Impact of subgrid-scale vertical turbulent mixing on eyewall asymmetric structures and mesovortices of hurricanes. Q. J. R. Meteorol. Soc. 140 (679), 416–438.
Zhu, P., Zhu, Z., Gopalakrishnan, S., Black, R., Marks, F.D., Tallapragada, V., Zhang, J.A., Zhang, X., Gao, C., 2015. Impact of sub-grid-scale processes on eyewall replacement cycle of tropical cyclones in HWRF system. Geophys. Res. Lett. 42 (22), 10–027.
Zhu, P., Tyner, B., Zhang, J.A., Aligo, E., Gopalakrishnan, S., Marks, F.D., Mehra, A., Tallapragada, V., 2019. Role of eyewall and rainband eddy forcing in tropical cyclone intensification. Atmos. Chem. Phys. 19 (22), 14289–14310.
Zhu, P., Hazelton, A., Zhan, Z., Marks, F.D., Tallapragada, V., 2021. The role of eyewall turbulent transport in the pathway to intensification of tropical cyclones. J. Geophy. Res. Atmos. 126 (17) https://doi.org/10.1029/2021JD034983 e2021JD034983.